Quadrotor Gray-Box Model Identification from High-Speed Flight Data

Sun, Sam; de Visser, Coen; Chu, Q. P.

DOI
10.2514/1.C035135

Publication date
2019

Document Version
Final published version

Published in
Journal of Aircraft: devoted to aeronautical science and technology

JOURNAL OF AIRCRAFT
Vol. 56, No. 2, March–April 2019

Quadrotor Gray-Box Model Identification from High-Speed Flight Data

Sihao Sun,* Coen C. de Visser,† and Qiping Chu‡
Delft University of Technology, 2629 HS Delft, The Netherlands

DOI: 10.2514/1.C035135

To explore the aerodynamic effects on a quadrotor in the high-speed flight regime and establish an accurate nonlinear model, free-flight tests with a quadrotor are carried out in a large-scale wind tunnel. The flight data reveal that complex aerodynamic interactions could appear and significantly influence the forces and moments acting on the quadrotor, which indicate the inaccuracy of state-of-art models established based on helicopter aerodynamic theory. To cope with this problem, gray-box models considering these effects are identified from flight data using a stepwise system identification approach, which combines both prior knowledge of rotorcraft aerodynamic properties as well as data observations. Previous models introduced in the literature are compared with the gray-box models. Validation results show an 80% reduction of moment model residuals and a 20% reduction of force model residuals.

Nomenclatures

A	=	regressor matrix
b, l, R	=	vehicle geometry parameters and rotor radius, m
C_h	=	horizontal force coefficient
C_t	=	thrust coefficient
$C_x, C_y, C_z, C_l, C_m, C_n$	=	aerodynamic forces and moments coefficients
$\hat{d}$	=	number of terms in $P^d(\boldsymbol{x})$
$\boldsymbol{F}, F_x, F_y, F_z$	=	aerodynamic forces, N
g	=	acceleration of gravity, m/s^2
I_p	=	inertia moment of the propeller, kg · m^2
I_v	=	inertia moment of the vehicle, kg · m^2
$\boldsymbol{M}, M_x, M_y, M_z$	=	aerodynamic moments, N · m
$\boldsymbol{M}_h, \boldsymbol{F}_h$	=	aerodynamic force and moment estimations from the hovering model, N and N · m, respectively
$\boldsymbol{M}_{I_p}$	=	rotor inertia-related moment
m	=	total mass of the vehicle, kg
N	=	number of rotors or number of measurement samples
n	=	dimension of $\boldsymbol{x}$
$P^d(\boldsymbol{x})$	=	set comprising all bases of the dth-order polynomial with $\boldsymbol{x}$ as the independent variable
$\bar{p}, \bar{q}, \bar{r}$	=	normalized body angular rates
R_{BG}	=	rotational matrix from the ground frame to the body frame
$\mathcal{S}(\cdot)$	=	candidate set
T	=	thrust, N
u, v, w	=	airspeed components in the body frame, m/s
u_p, u_q, u_r	=	control inputs for roll, pitch, and yaw
$\boldsymbol{V}, \boldsymbol{V}_g, \boldsymbol{V}_{\mathrm{wind}}$	=	airspeed, ground speed, and wind speed, m/s
$\boldsymbol{x}$	=	vector of model independent variables
$\boldsymbol{y}$	=	model outputs
$\boldsymbol{z}$	=	force and moment measurements
α, β	=	angle of attack and sideslip angle, rad
$\boldsymbol{\epsilon}$	=	model residual
$\boldsymbol{\theta}, \hat{\boldsymbol{\theta}}$	=	vector of model parameters and its estimation
κ_0, τ_0	=	force and torque coefficient of the hovering model, N · s and N · m · s
λ_r	=	damping rate in the hovering model, N · m · s
μ_h	=	horizontal advanced ratio
μ_x, μ_y, μ_z	=	advance ratios
$\bar{\nu}_{\mathrm{in}}$	=	normalized induced velocity
$\boldsymbol{\xi}$	=	regressor
ρ	=	air density, kg/m^3
σ	=	standard deviation
$\boldsymbol{\Omega}, p, q, r$	=	body angular rates, rad/s
Ω_i	=	rotation speed of the ith rotor, rad/s
$\bar{\Omega}$	=	geometric average of rotor speeds, rad/s
ω_i	=	normalized rotation speed of the ith rotor

Presented as Paper 2018-0523 at the 2018 AIAA Atmospheric Flight Mechanics Conference, Kissimmee FL, 8–12 January 2018; received 13 June 2018; revision received 31 August 2018; accepted for publication 31 August 2018; published online 24 November 2018.

*Ph.D. Student, Control and Simulation Section, Faculty of Aerospace Engineering, Kluyverweg 1.

†Assistant Professor, Control and Simulation Section, Faculty of Aerospace Engineering, Kluyverweg 1. Member AIAA.

‡Associate Professor, Control and Simulation Section, Faculty of Aerospace Engineering, Kluyverweg 1.

I. Introduction

MULTIROTOR drones are widely used currently as an efficient tool in multiple applications such as reconnaissance, package delivery, agriculture monitoring, filming, and even personal transportation. Multirotor drones are equipped with individual rotors producing both propulsion and control power, and they frequently operate in nonhovering conditions in outdoor environments. During flights with nonstatic incoming flow in these conditions, the aerodynamic characteristics of these rotors are different from those modeled in static conditions and considerable freestream induced aerodynamic effects become apparent.

Drones are able to operate in conditions in which additional aerodynamic effects occur without full knowledge of them due to the high update rates of sensors and the robustness of the controller [1–3]. However, knowledge of these effects will be necessary for controllers capable of fully exploring the flight envelope [4,5], such as high-speed flights with aggressive maneuvers. Next to the controller enhancement, the modeling of these aerodynamic effects is also desirable of providing better attitude estimation [6] and refining the design process [7]. In addition, full knowledge of these aerodynamic effects is also required for high-fidelity simulation platforms [8]; finally, global models need to be established for flight envelope computation [9], which is the main motivation for the current work.

The main subject of this research is the quadrotor, which is one of the simplest possible multirotor drones. The aerodynamic effects acting on quadrotors can be summarized as the force variation and moment variation, as compared to that in the hovering condition without ground effect. Several discussions about these forces and moment variations are present in the literature.

Most literature sources focus on improving the thrust model. Reference [10], for instance, elaborated on the cause of thrust variation during translational flight. The modeling process was mostly derived from helicopter aerodynamic theories. References [4,10,11] used the momentum theory to develop the model of relationships between thrust efficiency, flight speed, and the angle of attack. The thrust calculation of a single rotor according to the blade element theory was adopted [12–15]. The momentum theory and blade element theory were also combined, and a so-called blade element momentum theory was used to enhance the thrust model accuracy [16–18].

Drag forces, which are mostly defined in the blade plane of multirotor drones, are also discussed in the literature. The blade flapping effect is considered the main cause of drag force [10,15, 19–21]. According to Refs. [12,17,19,20], lift also induces an aerodynamic drag on the blade elements and generates a hub force perpendicular to the thrust. Besides the resistance caused by the rotor, the aerodynamic drag from the airframe is also considered [16], which is quadratic as related to the flight speed.

Compared to forces, moment variations have received less attention in the existing literature. The additional pitching moment due to the translational velocities was observed in the wind-tunnel test presented in Ref. [22]. In the trim condition during forward flight, the aft rotors rotated faster than the front rotor. The damping effects [21], blade stiffness [11], and drag forces [21] were considered to cause these moments as well. The bare airframe itself might also generate a pitching moment [8]. To the best of the authors' knowledge, no high-fidelity models of the aerodynamic moments exist in the literature.

Besides the forces and moments generated from the individual propellers and airframe, rotor–rotor and airframe–rotor interaction effects are suspected to greatly influence the aerodynamic forces and moments. Reference [13] showed that the interaction between multiple rotors deteriorated the total thrust from wind-tunnel tests. Reference [8] divided the forces and moments into propulsion, airframe, and interaction units; and the research of interaction terms is still ongoing. Models considering the interaction effect have been made [7,23], based on physical theory and engineering assumptions; however, they were not validated with in-flight data. The actual effects of these interactions on the thrust, drag, and moments remain largely unknown, which should be investigated with free-flight experiments.

The main contribution of this research is further revealing the effect of the aforementioned interactions from flight data and establishing accurate force and moment models taking account of these effects. To this end, multiple free-flight tests are carried out. Based on the data from these tests, it is shown that the interaction effects deteriorate the well-established thrust and drag model based on the first principles; in addition, they demonstrate significant inaccuracies in the pitch and rolling moment predictions obtained with the broadly accepted quadrotor hovering model, i.e., the distance of the propellers times their thrust differences. Furthermore, it is shown that the yawing moment is strongly influenced by the incoming flow during high-speed flight, which has not been discussed before.

To establish a high-fidelity model of forces and moments that is valid in a larger flight envelope, a system identification approach is used. Different from the first-principles modeling approach derived from helicopter aerodynamic theory, system identification methods are the proper choice for modeling these complex interaction effects. Specifically, a gray-box model is established that combines the information from prior physical knowledge of rotorcraft theory with experimental data obtained during high-speed flight, and it possesses both the reliability of physical theory and accuracy of observation.

Several system identification techniques can be applied to establish nonlinear gray-box models, depending on the structure of the model, such as polynomial functions, multivariate spline functions, neural networks, etc. Among them, a simple but effective piecewise polynomial structure is selected. A stepwise method is used for determining the model structure by selecting terms from a large set of candidate terms. This technique has been used in the past for full-scale aircraft system identification [24–26] but has never been used for determining the aerodynamic model of a quadrotor. The model structure candidates are determined from prior knowledge of rotorcraft aerodynamic theories as well as preliminary assumptions. The stepwise method selects candidates into the model in a stepwise scheme according to their contributions to the current model.

The identified models are compared with state-of-art force models considering aerodynamic effects as well as moment models established in hovering conditions. The validation results reveal around a 20% improvement in the accuracy of the force model and, more importantly, an over 80% improvement in the moment model in terms of the residual root mean square (RMS) in nonhovering conditions. Although these models are specific to the Bebop platform, the methodologies can be generalized to other multirotor platforms.

The flight experiments are carried out in the open jet facility (OJF), which is a large-scale wind tunnel with a 3 m aperture operated by the Delft University of Technology, as shown in Fig. 1. In contrast to static wind-tunnel tests, free flights are performed in the OJF in order to negate the disturbance effect of a force balance and, more importantly, to take dynamic motions into account. The wind tunnel provides a 2.5 by 2.5 by 5.0 m space to carry out these flights. A large number of different flight maneuvers are made to fully excite the system, and a maximum air speed up to 14 m/s is achieved. An off-the-shelf quadrotor (Parrot Bebop) running an open-source autopilot (Paparazzi) is used in these flights. The standard built-in inertia measurement unit (IMU) running at 512 Hz and external motion capture systems (Optitrack) running at 360 Hz are sensor-fused for data acquisition [27].

A normalization method for modeling multirotor drones in terms of dimensionless coefficients is proposed in this research. The dimensionless aerodynamic coefficients and states are analogous to those used for single rotorcraft. Moment coefficients are, for the first time, introduced for quadrotor drones, taking into account their multirotor characteristics. The gray-box model established will be presented in dimensionless form as a mapping between dimensionless states and force (moment) coefficients. These dimensionless coefficients are also useful for revealing the interaction effects, and even for comparing the aerodynamic properties of different drone models.

The paper is organized as follows. Section II introduces the coordinate definition and hovering model definition. Section III depicts the stepwise method and provides the definition of the dimensionless aerodynamic coefficients and other dimensionless variables related to the model. Section IV describes the flight test for this research and discusses the interaction effects observed from flight data. The identification process and results can be found in Secs. V and VI, respectively.

Fig. 1 Open jet facility, which is a large-scale wind tunnel, and the tested quadrotor.

II. Preliminary Modeling

A benchmark model is introduced in this section with the aim of further introducing the gray-box model and making comparisons between them. First, the two coordinate systems (in the form of the ground frame and the body frame) are defined (Fig. 2). For the ground frame, x_G is defined toward the wind-tunnel nozzle (in other words, into the freestream); and z_G is aligned with the gravity direction pointing downward. The body frame is fixed to the vehicle with the center of gravity at the origin. Also, x_B is aligned with the nose direction, y_B points to the right, and z_B points against the thrust direction.

The airspeed, which is the flight speed with respect to the airstream, is defined as

$$\boldsymbol{V} = \boldsymbol{V}_g - \boldsymbol{V}_{\text{wind}} \tag{1}$$

where $\boldsymbol{V}_g$ and $\boldsymbol{V}_{\text{wind}}$ indicate the ground speed and wind speed, respectively. The projection of airspeed on the body frame is expressed as $\boldsymbol{V} = [u \quad v \quad w]^T$. The angle of attack α and the sideslip angle $\boldsymbol{\beta}$ are defined as

$$\alpha = \arcsin(w/V) \qquad \beta = \arcsin\left(v/\sqrt{v^2+u^2}\right) \tag{2}$$

where $V = \|\boldsymbol{V}\|$. Note that, because the quadrotor is able to hover and reverse, these two angles are singular when the airspeed equals zero.

Rotor speeds (in radians per second) are expressed as $[\Omega_1 \quad \Omega_2 \quad \Omega_3 \quad \Omega_4]$, respectively. Figure 2 shows the rotor index and the rotation directions of the Parrot Bebop quadrotor, which is the object to be modeled in this paper.

For simplicity, the quadrotor is regarded as a rigid body, for which the translational and rotational dynamic equations can be written as

$$\dot{\boldsymbol{V}} + \boldsymbol{\Omega} \times \boldsymbol{V} = R_{\text{BG}}\boldsymbol{g} + \boldsymbol{F}/m \tag{3}$$

$$I_v\dot{\boldsymbol{\Omega}} + \boldsymbol{\Omega} \times I_v\boldsymbol{\Omega} = \boldsymbol{M} + \boldsymbol{M}_{I_p} \tag{4}$$

where $\boldsymbol{g} = [0 \quad 0 \quad g]^T$ indicates the gravity vector expressed in the ground frame. $\boldsymbol{\Omega} = [p \quad q \quad r]^T$ represents the angular velocity expressed in the body frame. The aerodynamic forces and moments are denoted as $\boldsymbol{F}$ and $\boldsymbol{M}$, respectively, which are expressed in the body frame as well. R_{BG} is the rotational matrix from the ground frame to the body frame. I_v stands for the inertia matrix, and m indicates the mass of the vehicle. $\boldsymbol{M}_{I_p}$ represents the moments due to gyroscopic effects and rotor spinup torque; the latter has been found to significantly influence the Bebop quadrotor [28]:

$$\boldsymbol{M}_{I_p} = \begin{bmatrix} qI_p(-\Omega_1 + \Omega_2 - \Omega_3 + \Omega_4) \\ pI_p(\Omega_1 - \Omega_2 + \Omega_3 - \Omega_4) \\ I_p(-\dot{\Omega}_1 + \dot{\Omega}_2 - \dot{\Omega}_3 + \dot{\Omega}_4) \end{bmatrix} \tag{5}$$

The positioning of a quadrotor in three-dimensional space is controlled by changing its attitude and total thrust. The attitude can be changed by differential thrust. Specifically, the rotor speed difference between the front and aft rotors produces a pitching moment, whereas a rolling moment can be produced by differential thrust between the left and right rotors. The rotor reaction torque is used to generate a yawing moment, which the quadrotor uses to control its heading.

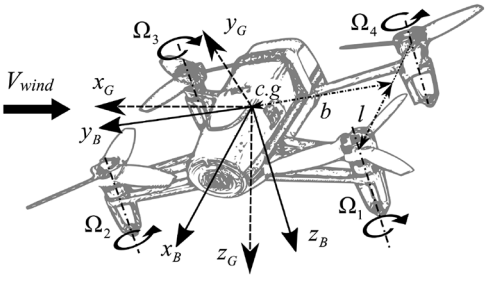

Fig. 2 Coordinate systems definition and sketch of Parrot Bebop quadrotor.

The emphasis of modeling is on the aerodynamic force vector $\boldsymbol{F}$ and the aerodynamic moment vector $\boldsymbol{M}$. Before establishing a gray-box model for $\boldsymbol{F}$ and $\boldsymbol{M}$, a hovering model that is only valid in hovering condition is introduced as a benchmark for comparison:

$$\boldsymbol{F}_h = \begin{bmatrix} 0 \\ 0 \\ -\kappa_0 \sum \Omega_i^2 \end{bmatrix} \tag{6}$$

$$\boldsymbol{M}_h = \begin{bmatrix} b\kappa_0(\Omega_1^2 - \Omega_2^2 - \Omega_3^2 + \Omega_4^2) \\ l\kappa_0(\Omega_1^2 + \Omega_2^2 - \Omega_3^2 - \Omega_4^2) \\ \tau_0(-\Omega_1^2 + \Omega_2^2 - \Omega_3^2 + \Omega_4^2) + \lambda_r r \end{bmatrix} \tag{7}$$

where l and b are geometry parameters of the quadrotor, as Fig. 2 shows. Note that κ_0, τ_0, and λ_r are constant coefficients. Note that the aerodynamic forces and moments are expressed in the body frame in this paper. Therefore, the third component of $\boldsymbol{F}_h$ is equal to the negative of the total thrust. Meanwhile, the first two components of $\boldsymbol{F}_h$ equal zero, which means that the rotor in-plane forces (i.e., drag forces) are neglected.

However, significant in-plane drag has been found [6,12,17,19], and thrust varies with the flight speed beyond the hovering regime [11]. Furthermore, aerodynamic moments are found to be completely different from what the hovering model predicts. These studies indicate the importance of finding a model that is valid in a larger flight envelope.

In this paper, a gray-box model is identified from high-speed free-flight data obtained in a wind tunnel. The aerodynamic effects of individual rotors, the rotor–rotor, and the rotor–airframe aerodynamic interactions in high-speed conditions are considered in this gray-box model as well.

III. Methodologies

A. Nondimensionalization

Dimensionless aerodynamic coefficients are convenient for comparisons between different conditions and platforms. For a single rotor, forces and moments can be normalized by rotor speed and reference area [8]. However, for multirotor aircraft such as quadrotors, determining the aerodynamic coefficient of each rotor could be impracticable using a system identification approach because only joint forces are measurable by the three-axis accelerometer located at the center of gravity. Furthermore, the local airspeed differs between rotors because of complex aerodynamic interactions, which make the rotor-by-rotor modeling approach impractical.

In this research, a novel nondimensionalization approach is proposed that is based on an assumption that aerodynamic forces and moments are mainly generated by the rotor system. A geometric average of rotor speeds is used to represent the effect of multirotors:

$$\bar{\Omega} = \sqrt{\frac{\sum_{i=1}^{N} \Omega_i^2}{N}} \tag{8}$$

where N is the number of rotors and equals four for the quadrotor. In most cases, rotors are the same size with radius R. Afterward, forces and moments acting on the entire vehicle can be normalized by the average rotor speed:

$$C_z = \frac{F_z}{\rho(N\pi R^2)(R\bar{\Omega})^2}, \quad C_x = \frac{F_x}{\rho(N\pi R^2)(R\bar{\Omega})^2}, \quad C_y = \frac{F_y}{\rho(N\pi R^2)(R\bar{\Omega})^2} \tag{9}$$

$$C_l = \frac{M_x}{\rho b(N\pi R^2)(R\bar{\Omega})^2}, \quad C_m = \frac{M_y}{\rho b(N\pi R^2)(R\bar{\Omega})^2},$$
$$C_n = \frac{M_z}{\rho b(N\pi R^2)(R\bar{\Omega})^2} \tag{10}$$

where b is the reference length chosen arbitrarily as long as it represents the geometric size of a specific vehicle. Because F_z is opposite to thrust, which brings intuitive inconvenience, $T = -F_z$ is used as the total thrust force and $C_t = -C_z$ as the thrust coefficient. Note that T is interpreted as the joint of the rotor thrust and drag force along the body vertical axis.

Translational and angular velocities, which have been found to significantly influence the aforementioned coefficients [10,19], are normalized by

$$\mu_x = \frac{u}{\bar{\Omega}R}, \quad \mu_y = \frac{v}{\bar{\Omega}R}, \quad \mu_z = \frac{w}{\bar{\Omega}R} \tag{11}$$

$$\bar{p} = \frac{pb}{\bar{\Omega}R}, \quad \bar{q} = \frac{qb}{\bar{\Omega}R}, \quad \bar{r} = \frac{rb}{\bar{\Omega}R} \tag{12}$$

The horizontal component of the advance ratio $\mu = \sqrt{\mu_x^2 + \mu_y^2 + \mu_z^2}$, which is defined as $\mu_h = \sqrt{\mu_x^2 + \mu_y^2}$, is used to analyze interaction effects in this research. These dimensionless parameters are analogous to those used for single-rotor aircraft.

The rotor speeds are normalized by

$$\omega_i = \frac{\Omega_i}{\bar{\Omega}} \tag{13}$$

It is assumed that $\bar{\Omega} > 0$ always holds to avoid the singularity because the status that all rotors are stopped is out of the scope of this paper.

The moments for controlling attitude are produced by differential thrust from rotor speeds differences. Here, three normalized inputs for roll, pitch, and yaw controls are defined

$$u_p = (\omega_1^2 + \omega_4^2) - (\omega_2^2 + \omega_3^2) \tag{14}$$

$$u_q = (\omega_1^2 + \omega_2^2) - (\omega_3^2 + \omega_4^2) \tag{15}$$

$$u_r = -(\omega_1^2 + \omega_3^2) + (\omega_2^2 + \omega_4^2) \tag{16}$$

where signs and numbers are in accordance with the definition in Fig. 2, which may change for different types of quadrotor vehicles.

B. Stepwise System Identification

This section introduces the system identification approach applied to establish the gray-box model. Specifically, a regression method together with a model structure selection algorithm is used for determining mappings from dimensionless states to aerodynamic force and moment coefficients. The relation of model outputs to measurements satisfies

$$\boldsymbol{z} = \boldsymbol{y} + \boldsymbol{\epsilon} = A\boldsymbol{\theta} + \boldsymbol{\epsilon} \tag{17}$$

where $\boldsymbol{z} \in \mathbb{R}^N$ stands for N measured dimensionless forces and moments. Also, $\boldsymbol{y} = A\boldsymbol{\theta}$ denotes the model output and the $\boldsymbol{\epsilon} \in \mathbb{R}^N$ vector indicates model residuals. $A \in \mathbb{R}^{N\times p}$ is the regressor matrix with each column as a regressor, which is an arbitrary combination of independent variables. Note that $\boldsymbol{\theta} \in \mathbb{R}^p$ stands for the parameters of regressors to be estimated using, e.g., an original least-square estimator:

$$\hat{\boldsymbol{\theta}} = (A^T A)^{-1} A^T \boldsymbol{z} \tag{18}$$

where $\hat{\boldsymbol{\theta}}$ is the optimal parameter estimation that minimizes the sum of squares of the residual $\boldsymbol{\epsilon}$. The process of model structure selection is concerned with the choice of particular regressors in the A matrix.

In this paper, two steps are taken in the model structure selection. The first step is defining candidate regressors set using prior knowledge; and the second step is selecting candidates using a selection algorithm.

A method to rigorously define candidate sets is introduced. Supposing $y(x_1, x_2, x_3)$ is a model with three independent variables and an unknown model structure, the candidate set of y can be denoted by $\mathcal{S}(y)$. In this research, the model structures are in the form of polynomial functions. Now, denote the basis of a dth-order polynomial function of $\boldsymbol{x} = (x_1, x_2, x_3)$ as $P^d(\boldsymbol{x})$, and then the candidate set consisting of arbitrary polynomial terms can be defined. For example, if

$$\mathcal{S}(y) = \{P^2(x_1, x_2), P^2(x_1, x_2)x_3\}$$

the candidate set of y contains regressors from

$$P^2(x_1, x_2) = \{x_1, x_2, x_3, x_1^2, x_2^2, x_1x_2\}$$

and from

$$P^2(x_1, x_2)x_3 = \{x_1x_3, x_2x_3, x_3x_3, x_1^2x_3, x_2^2x_3, x_1x_2x_3\}$$

Define the multiplication of two sets as a set containing nonrepetitive products of elements from the two sets:

$$\{a_1, a_2 \ldots, a_m\}\{b_1, b_2 \ldots, b_n\} = \{a_1b_1, \ldots a_1b_n, a_2b_1, \ldots, a_2b_n, \ldots, a_mb_1, \ldots, a_mb_n\} \tag{19}$$

Then, $\mathcal{S}(y)$ can be expressed in a simplified form according to the law of association:

$$\mathcal{S}(y) = \{P^2(x_1, x_2), P^2(x_1, x_2)x_3\} = \{P^2(x_1, x_2)\{1, x_3\}\} \tag{20}$$

A general formulation of $P^d(\boldsymbol{x})$ is

$$p^d(x_1, x_2, \ldots, x_n) = \left\{\prod_{i=1}^{n} x_i^{k_i} | 0 \le \sum_{i=1}^{n} k_i \le d, k_i \in \{0, 1, 2, \ldots, d\}\right\} \tag{21}$$

of which the total number of elements can be calculated by

$$\hat{d} = \frac{(d+n)!}{n!d!} \tag{22}$$

After determining the candidate set, a so-called (forward–backward) stepwise regression algorithm is applied to select regressors to build the model. The algorithm is summarized in Appendix A. Readers may refer to Ref. [25] for more details.

IV. Data Acquisition and Analysis

A. Experimental Setup

To identify force and moment models in high-speed flight regimes, free flights are performed in a large-scale wind tunnel for data acquisition. The tested quadrotor is Parrot Bebop without bumpers, as Fig. 2 shows. The native autopilot of this off-the-shelf drone is replaced by Paparazzi,[§] which is an open-source autopilot that runs at 512 Hz and is capable of performing aggressive maneuvers. The incremental nonlinear dynamic inversion guidance law and attitude controller have been programmed in Paparazzi [3,28] to guarantee the position tracking performance against strong wind, which is essential for flight tests in our research. The quadrotor is equipped with a closed-loop brushless dc motor controller: an MPU6050 inertia measurement unit including a three-axis accelerometer and gyroscope. The inertia of Bebop is measured using the approach introduced in Ref. [29] with a percent error of less than 5%. The parameters of the tested quadrotor are listed in the Table 1.

Flight tests are performed in the open jet facility, which is a large-scale wind tunnel operated by Delft University of Technology. The drone is controlled to maneuver in a confined area that is

[§]Data available online at https://github.com/paparazzi/paparazzi [retrieved 04 March 2017].

Table 1 Inertia and geometric parameters of Parrot Bebop

m , kg	$I_{v,xx}$, kg · m^2	$I_{v,yy}$, kg · m^2	$I_{v,zz}$, kg · m^2	$I_{v,xz}$, kg · m^2	I_p , kg · m^2	b , m	l , m	R , m
0.389	0.000906	0.001242	0.002054	1.42E − 05	3.39E − 06	0.0775	0.0975	0.064

approximately 5.0 m long, 2.5 m wide, and 2.5 m high. The wind speed is varied from 0 to 14 m/s with 2 m/s intervals to simulate flights at different airspeeds. An external motion capture system is applied to measure the velocities and positions of the drone for indoor navigation. As Fig. 3 shows, five waypoints in the flight area are set to conduct flight maneuvers. To perform longitudinal maneuvers, the quadrotor can be controlled to track points A and B alternately. Similarly, waypoints C and D are set for performing the lateral maneuver. To perform vertical maneuvers during forward flight, the drone is controlled to stay at point O and climb or descend in 2 m/s. Longitudinal, lateral, and vertical maneuvers are conducted at varying heading angles denoted by ψ, which are defined in Fig. 3; the heading angle is increased from 0 to 360 deg in steps of 45 deg. To identify the yawing moment model considering aerodynamic effects, yaw maneuvers are carried out at point O by changing ψ in steps of 45 deg both clockwise and counterclockwise. Forward and backward flights are conducted by tracking points A and B by turns. Lateral flights are performed between C and D. Descend and ascend flights, as well as yaw maneuvers, are made at point O. The heading angle ψ is defined as the angle between x_B and x_G (clockwise positive).

B. Data Preprocessing

Flight data for system identification are collected by onboard and external sensors. Specifically, rotor speeds are observed by the motor controller; and angular rates and specific forces are measured by the gyroscope and accelerometer, respectively. These measurements are logged on board at 512 Hz. The external motion capture system (10× OptiTrack Prime 17 W cameras) measured the position of six markers fixed on the vehicle at 360 Hz, with a standard deviation of less than 0.2 mm. Henceforth, the quadrotor position, attitude, and ground speed are derived from these marker positions and resampled to 512 Hz to align with onboard measurements.

Measurements from the two sources have been fused using an extended Kalman filter with the aim of calculating the IMU bias [27]. The unbiased IMU measurements are further filtered by a fourth-order Butterworth low-pass filter. The power spectral density (PSD) of the accelerometer and gyroscope measurements from one flight are plotted in Fig. 4. There is a resonance peak at around 120 Hz, which is most likely caused by rotor imbalance (rotors rotate at around 7000 rpm = 117 Hz). Circled parts indicate the noise caused by an unbalanced rotor, which is inevitable. Filter cutoff frequencies are chosen as 5 and 16 Hz, respectively, leading to a considerable noise reduction as shown in Fig. 5.

Finally, force and moment measurements are derived from the processed IMU data. The specific force times the mass of the quadrotor equals the resultant nongravitational force, namely, $\boldsymbol{F}$. The moment $\boldsymbol{M}$ can be obtained from Eq. (4), where the angular velocity $\boldsymbol{\Omega}$ is obtained from the processed gyroscope measurement.

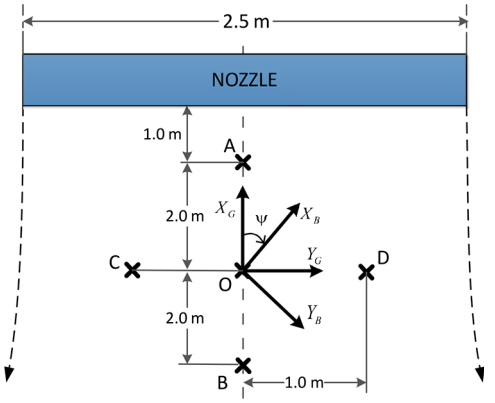

Fig. 3 Top view diagram of flight maneuvers performed in the wind tunnel.

C. Complex Aerodynamic Effect

As outlined in the Introduction (Sec. I), complex aerodynamic effects (such as interactions between quadrotor components) have been clearly observed from the flight-test data. These effects can significantly affect external forces and moments and have to be taken into account when creating a high-fidelity model.

Thrust coefficients C_t and corresponding sideslip angles β are shown in Fig. 6. These data are divided into three groups according to angles of attack α. The intervals of α are presented in the figure as well, whereas the interval of the advance ratio is set as $\mu \in [0.1, 0.11]$ ($V \approx 5$ m/s). Note that only data within these intervals are plotted. Trend lines are also given for a better illustration of the C_t variation in different β. Apart from the vertical shift of C_t, the effect of β on C_t also varies with α. When α is negative with a large absolute value, the mean value of C_t seems uncorrelated to β. As α is approaching zero, data with larger $|\beta|$ have smaller C_t, which could be interpreted as the thrust degradation caused by disturbance from the fuselage of the Bebop quadrotor in high sideslip flights when the aft rotors are within the fuselage wake. In contrast, when α is decreased and becomes

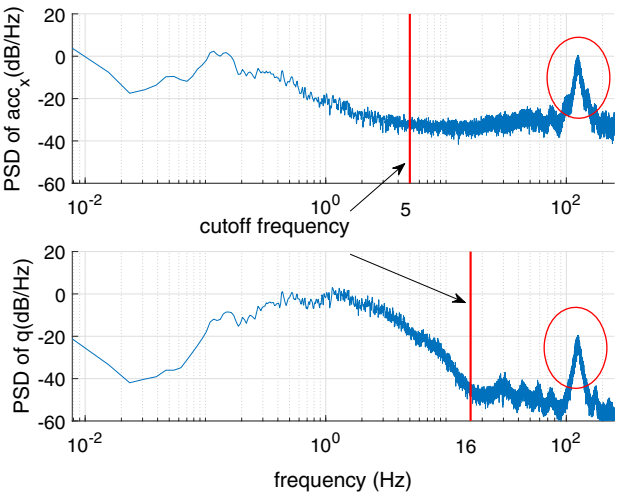

Fig. 4 Power spectrum density of accelerometer measurement and gyroscope measurement (acc_x and q) by Welch's method in MATLAB.

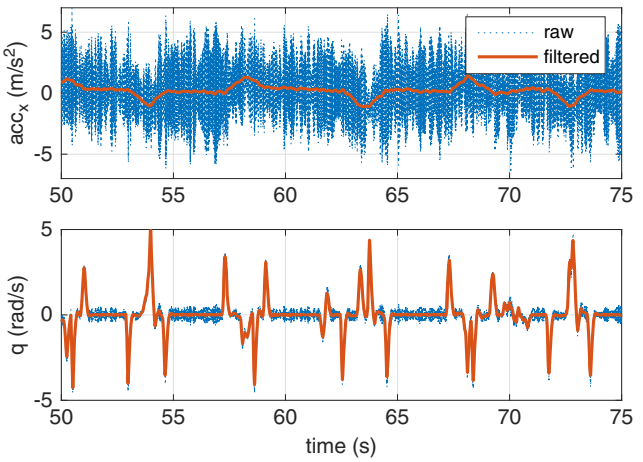

Fig. 5 Comparison between raw and filtered measurements from the accelerometer (acc) and gyroscope.

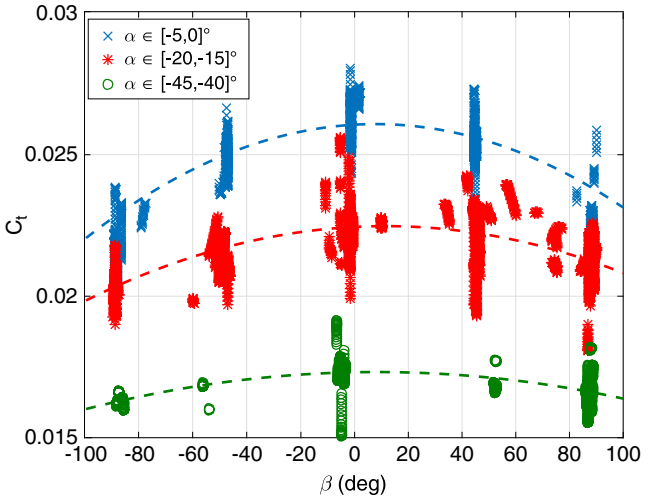

Fig. 6 C_t vs sideslip angle in different angles of attack.

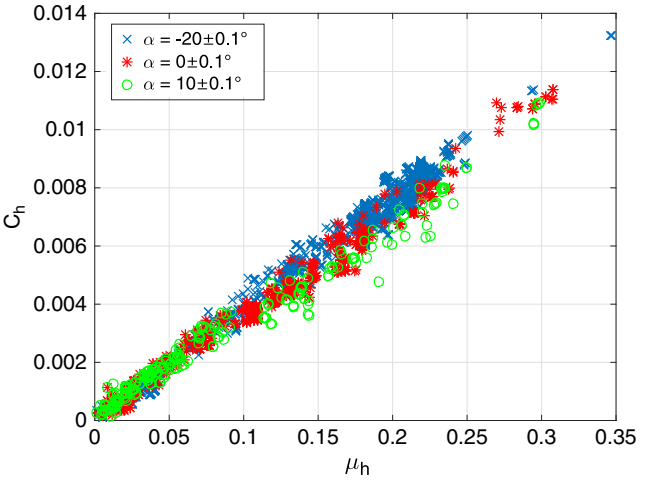

Fig. 8 C_h vs μ_h in different angles of attack when sideslip angle is $\beta \in [-10, 10]$ deg. A larger angle of attack can reduce the horizontal force coefficient.

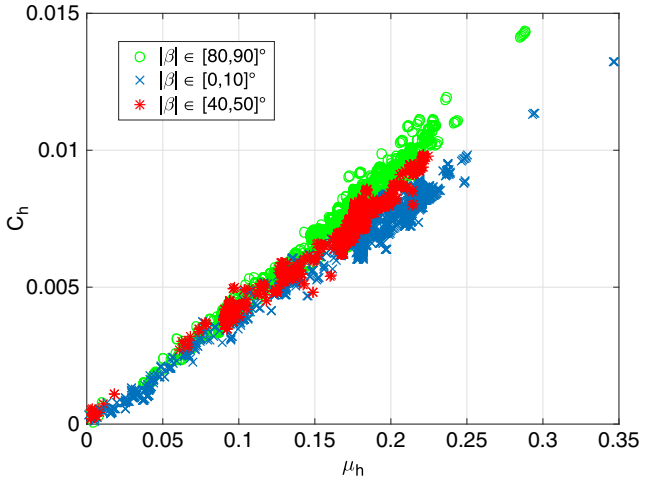

Fig. 7 C_h vs μ_h in different sideslip angle intervals. Plot shows horizontal force coefficient varies with respect to sideslip angle.

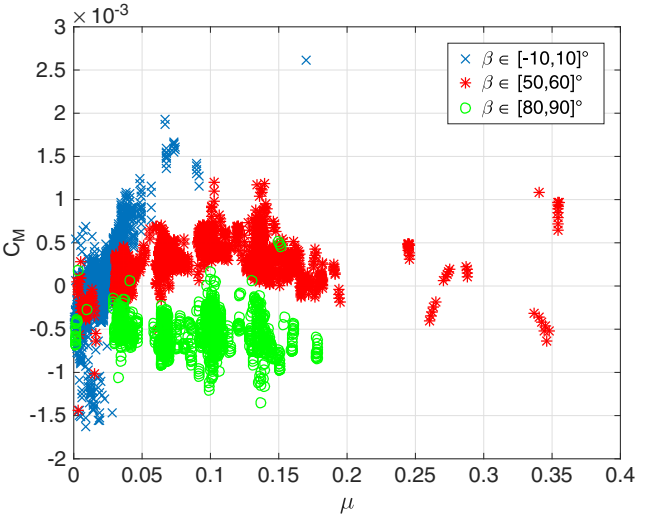

Fig. 9 C_m in different sideslip angles when $u_q \in [-0.05, 0]$. Large noseup moment can be observed when sideslip angle is small ($\beta \in [-10, 10]$ deg).

sufficient small, the aft rotors are outside the fuselage wake; therefore, the sideslip angle does not influence the thrust coefficient. During the experiment, a clear shrill sound was produced while the aft rotors were obstructed by the fuselage, which can be regarded as additional evidence that supports this hypothesis.

Figure 7 presents the horizontal force coefficient defined as $C_h = \sqrt{C_x^2 + C_y^2}$, which indicates the total aerodynamic resistance projected on the x_B–y_B plane. The angle of attack is selected to be around -20 deg, which is typical during forward flight. The distribution of data points with a small sideslip angle ($|\beta| \in [0, 10]$ deg) shows an almost linear relationship between C_h and the horizontal advance ratio μ_h. As the sideslip angle grows, the drag coefficient also increases; when $|\beta| \in [80, 90]$ deg, a quadratic tendency appears. This may be due to the fact that the fuselage of the Bebop has a larger projection area on the y_B direction, as Fig. 2 shows.

Besides the sideslip angle, the angle of attack also affects C_h. Because a large portion of the drag is produced by the rotors, thrust degradation caused by aerodynamic interactions can lead to induced drag reduction, and subsequently decrease the total drag force. This drag reduction is not only observed in the large sideslip angle but in also straightforward flights when the fuselage wake does not influence rotors. As can be seen in Fig. 8, in which the sideslip angle is small ($\beta \in [-10, 10]$ deg) however, C_h is found reduced when α is close to or above zero. This might be explained by the fact that the front rotors can obstruct the aft rotors and degrade their aerodynamic characteristics as well. Note that this drag force reduction is not obvious in the low-speed region because the flight speed is not high enough for this interaction. The drag force variance due to interactions should be considered as well in a high-fidelity model.

Figure 9 presents the pitching moment coefficient C_m versus the advance ratio μ at different sideslip angles. Significant differences can be found in different β intervals. For these data, the pitch control u_q are chosen close to zero ($u_q \in [-0.05, 0]$), which means that almost no pitching moment is present in the hovering condition because the front and aft rotors are nearly at the same speed. It is evident that the pitching moment increases significantly as the flight speed grows when $|\beta| \in [-10, 10]$ deg as compared to other sideslip angles. This pitchup moment might be caused by blade flexibility [11] or interactions between rotors.

The angle of attack is found to be positively related to the pitching moment during forward flight. Figure 10 shows the data and trend lines of C_m versus α with $u_q \in [-0.01, 0.01]$ and $\beta \in [-10, 10]$ deg. In these cases, the aft rotors and front rotors have almost the same rotor speeds. In general, C_m is positively correlated with the angle of attack, indicating the longitudinal instability of a quadrotor. The slope is larger with a higher advance ratio, which is consistent with the results given by Fig. 9. More important, the C_m is almost always positive, indicating that a noseup aerodynamic moment appears in quadrotor forward flight even with a large negative angle of attack. This coincides with the result from Ref. [22] that the aft rotors need to rotate much faster than the front rotors in trim conditions. Similarly, for instance, flying to the right (with $\beta = 90$ deg) can produce a

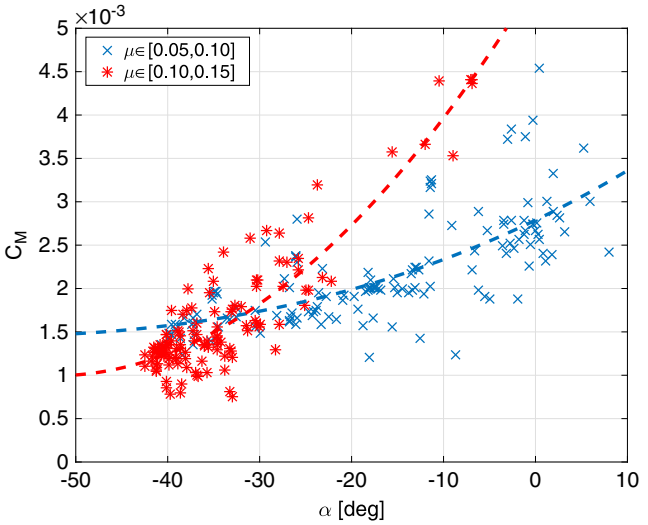

Fig. 10 C_m vs α in different advance ratio intervals with $u_q \in [-0.01, 0.01]$ and $\beta \in [-10, 10]$ deg.

negative rolling moment that requires the left rotors to rotate faster in order to keep balance. This phenomenon is strongly present in the data; simple hovering models that neglect this effect will produce highly inaccurate moment predictions in fast flight regions.

The yawing moment is also found to be influenced by the sideslip angle. Notate the difference between the measured yawing moment and that calculated by the hovering model by ΔM_z, which is regarded as the additional yawing moment due to the aerodynamic effects:

$$\Delta M_z = M_z - [\tau_0(-\Omega_1^2 + \Omega_2^2 - \Omega_3^2 + \Omega_3^2) + \lambda_r r] \tag{23}$$

As is shown in Fig. 11, ΔM_z is negatively related to the sideslip angle in general. When $|\beta| < 40$ deg, ΔM_z is in the vicinity of zero. However, its dispersion suddenly increases when $|\beta| < 40$ deg. At the same time, one aft rotor starts to be obstructed by the fuselage. The airframe–rotor aerodynamic interaction might occur in this situation as the cause of the sudden increased yawing moment.

V. Quadrotor Model Structure Candidates

This section introduces the determination of candidate structure sets for the quadrotor dimensionless aerodynamic force and moment models, based on prior physical knowledge and observations. Then, the stepwise regression algorithm can be carried out to obtain the final model structure, which will be presented in a subsequent section.

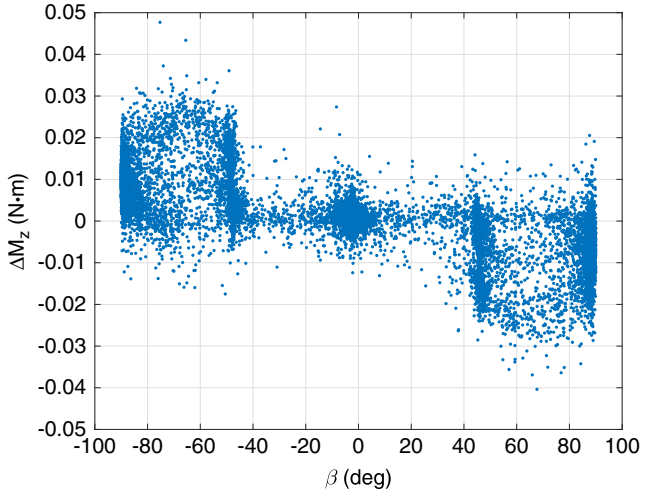

Fig. 11 Additional aerodynamic yawing moment ΔM_z with respect to the hovering model. ΔM_z is negative related to the sideslip angle, indicating that an aerodynamic moment related to β exists.

A. Force Model Candidates

F_x and F_y denote forces perpendicular to the thrust direction brought by aerodynamic resistance, of which the lift-induced drag and the blade flapping effect are the two major causes [6,12,19]. A widely accepted drag model of a single rotor is [6,12]

$$F_{x,i} \propto u_i \Omega_i \tag{24}$$

where $F_{x,i}$ and u_i stand for the in-plane force and local velocity of the ith rotor on the x_b direction, respectively. In addition, as Sec. IV.C showed, the airframe affected the drag force as well, especially at large sideslip angles. Therefore, the square of the velocity has been added into the drag model [16]. The drag force on the x_B direction can thus be expressed as

$$F_x = \kappa_{d,1} \sum_{i=1}^{4} \Omega_i u_i + K_{d,2} u^2 \tag{25}$$

where $\kappa_{d,1}$ and $\kappa_{d,2}$ are constants. Recalling Eqs. (8), (9), and (11), the normalized form of Eq. (25) can be obtained:

$$C_x = C_{x,1}\mu_x + C_{x,2}\mu_x^2 \tag{26}$$

Note that the rotor speed term in Eq. (25) disappears after normalization. This process needs to replace the arithmetic mean of rotor speeds by their geometrical mean, which does not lose accuracy in most flight conditions (0.8% relative error on average).

The preceding model can produce accurate predictions in most low-speed cases. However, it loses accuracy when interaction effects appear. For comparison with the gray-box model established in this research, the drag model in Eq. (26) is named the *reduced model*.

An additional term $C_{x,2,(\mu_x,|\mu_y|,\mu_z)}$, of which the exact structure is to be determined, is added to the reduced model. The viables in the subscript parentheses indiate the independent variables of $C_{x,2}$. A preliminary model structure of C_x can be

$$C_x = C_{x,1}\mu_x + C_{x,2,(\mu_x,|\mu_y|,\mu_z)} \tag{27}$$

Note that the $C_{x,2}\mu_x^2$ term is moved into the second term because it has a negligible effect in the flight regime, as the data show.

Recall the observation in the Sec. IV.C; β, α, and μ_h greatly influence the drag coefficient. Singularities in α and β, however, could occur in hovering conditions; therefore, three components of the advance ratio are chosen as the independent variables. Absolute values of μ_y are used due to the symmetry of the quadrotor.

Similarly, for C_y, we have

$$C_y = C_{y,1}\mu_y + C_{y,2,(|\mu_x|,\mu_y,\mu_z)} \tag{28}$$

The stepwise regression algorithm can be applied to determine the exact structure of the unknown parts of the aforementioned models. The candidate sets of C_x and C_y are chosen as

$$\mathcal{S}(C_x) = \{P^3(\mu_x, |\mu_y|, \mu_z)\} \tag{29}$$

$$\mathcal{S}(C_y) = \{P^3(|\mu_x|, \mu_y, \mu_z)\} \tag{30}$$

The terms μ_x and μ_y are always the first candidates to be tested by the model structure selection algorithm when assembling, respectively, the models for C_x and C_y.

F_z is derived by taking account of the thrust variation. In general, the thrust of the ith rotor with a constant pitching angle can be expressed as [30]

$$T_i = \frac{\rho a B c \omega_i^2 R^3}{2}\left(\frac{\theta_r}{3} + \frac{(u_i^2 + v_i^2)\theta_r}{2\omega_i^2 R^2} + \frac{-w_i + \nu_{\text{in},i}}{2\omega_i R}\right) \tag{31}$$

where a is the lift curve slope of the blade profile, B represents the number of blades, c is the blade chord length, and θ_r stands for the

rotor pitch angle. These parameters are related to rotor design; they normally are all constants for quadrotors. Also, $\nu_{\text{in},i}$ indicates the induced velocity of the i^{th} rotor.

A common way to model F_z is projecting the thrust of four rotors on the body frame and assuming that local velocities and induced velocities of the rotors are identical, yielding

$$F_z = -\sum_{i=1}^{4} T_i = \kappa_{t,1}\sum_{i=1}^{4}\Omega_i^2 + \kappa_{t,2}(u^2+v^2) + \kappa_{t,3}(-w+\nu_{\text{in}})\sum_{i=1}^{4}\Omega_i \quad (32)$$

where $\kappa_{t,1}$, $\kappa_{t,2}$, and $\kappa_{t,3}$ are constants. Equation (32) is the model structure adopted in several studies [13,30]; it is indicated as the reduced model to compare against the new gray-box model. A dimensionless form of Eq. (32) can be calculated by substituting Eqs. (8), (9), and (11) into Eq. (32), yielding

$$C_z = C_{z,0} + C_{z,1}(\mu_x^2+\mu_y^2) + C_{z,2}(-\mu_z+\bar{\nu}_{\text{in}}) \quad (33)$$

where $C_{z,0}$, $C_{z,1}$, and $C_{z,2}$ are constants. Note that $\bar{\nu}_{\text{in}}$ indicates the dimensionless induced velocity normalized by $\bar{\Omega}R$. The induced velocity $\bar{\nu}_{\text{in}}$ can be calculated by [4]

$$\bar{\nu}_{\text{in}} = \frac{C_{t,h}}{2\sqrt{\mu_x^2+\mu_y^2+(-\mu_z+\bar{\nu}_{\text{in}})^2}} \quad (34)$$

where $C_{t,h}$ is the thrust coefficient in the hover case, which can be estimated accurately by conducting hovering flight experiments.

As mentioned earlier, interaction effects could degrade rotor thrust. This effect is not considered in the reduced model [Eq. (32)]: not to mention other unknown complex aerodynamic effects and drag force on the z_B direction. The deviation of C_z from these effects is denoted by $C_{z,3}$. The flight speed, the difference between aft and front rotors, and vehicle angular velocities could be the individual variables of this unknown part. Thus, a gray-box model of C_z can be formalized as

$$C_z = C_{z,0} + C_{z,1}(\mu_x^2+\mu_y^2) + C_{z,2}(-\mu_z+\bar{\nu}_{\text{in}}) + C_{z,3,(|\mu_x|,|\mu_y|,\mu_z,|u_p|,|u_q|,|u_r|,|p|,|q|,|r|)} \quad (35)$$

Henceforth, the stepwise regression algorithm is applied to determine the structure of C_z, of which the candidate structure set is chosen as

$$\mathcal{S}(C_z) = \{P^4(|\mu_x|,|\mu_y|,\mu_z)\{1,|\bar{p}|,|\bar{q}|,|\bar{r}|,|u_p|,|u_q|,|u_r|\}\} \quad (36)$$

Note that $(\mu_x^2+\mu_y^2)$ and $(-\mu_z+\bar{\nu}_{\text{in}})$ are regarded as fixed regressors that have been added in the model before the selection.

Both the reduced model and the gray-box model can be established using the system identification method. Table 2 briefly compares the procedures of establishing these models.

B. Moment Model Candidates

Compared to the hovering case, additional aerodynamic moments can be produced during high-speed flight. First, the pitching moment could be a result of rotor resilience and the blade flapping effect [11]. Second, the vertical distance between rotor planes and the center of gravity also brings moments due to rotor drag [21]. Third, the angular rate (dynamic) damping term also contributes to the total aerodynamic moment [21]. Fourth, as was observed from the flight-test data, aerodynamic interactions may degrade the thrust of the aft rotors and lead to additional pitchup moments. All the aforementioned factors are related to the advance ratio and angular rates.

Taking account of these possible effects, a lumped model of the pitching moment coefficient C_m could be expressed as

$$C_m = C_{m,(\mu_x,\mu_y,\mu_z,\bar{q},u_q)} \quad (37)$$

with the advance ratio, the dimensionless pitch rate, and the pitch input as independent variables.

The preceding pitch model neglects the influence of lateral variables u_p, u_r, p, and r, which are of less effect on the pitching moment based on the flight data. However, μ_y is included in the model to handle the sideslip effect. To further simplify the candidate set, u_q and $\bar{q}$ are assumed linearly related to the pitching moment. Thus, the lumped model [Eq. (37)] can be expressed as

$$C_m = C_{m,0,(\mu_x,|\mu_y|,\mu_z)} + C_{m,u_q,(\mu_x,|\mu_y|,\mu_z)}u_q + C_{m,q,(\mu_x,|\mu_y|,\mu_z)}\bar{q} \quad (38)$$

Based on the structure in Eq. (38), the candidate set of C_m is chosen as

$$\mathcal{S}(C_m) = \left\{P^5(\mu_x,\mu_z)P^2(|\mu_y|)\{1,\bar{q},u_q\}\right\} \quad (39)$$

The preliminary structure of the rolling moment model can be similarly determined as

$$C_l = C_{l,0,(|\mu_x|,\mu_y,\mu_z)} + C_{l,u_p,(|\mu_x|,\mu_y,\mu_z)}u_p + C_{l,p,(|\mu_x|,\mu_y,\mu_z)}\bar{p} \quad (40)$$

of which the regressors are selected from the candidate set

$$\mathcal{S}(C_l) = \left\{P^5(\mu_y,\mu_z)P^2(|\mu_x|)\{1,\bar{p},u_p\}\right\} \quad (41)$$

The yawing moment model is found to be much more complicated, and u_r may not be linear to the model. Thus, a preliminary structure is determined as

$$C_n = C_{n,(\mu_x,\mu_y,\mu_z,\bar{r},u_r)} \quad (42)$$

of which the candidate set is chosen as

$$\mathcal{S}(C_n) = \left\{P^5(\mu_x,\mu_y,\mu_z)P^3(\bar{r})P^3(u_r)\right\} \quad (43)$$

VI. Results

A. Model Estimation Results

After defining candidate structure sets, all force and moment models are determined by the stepwise regression algorithm. This section provides the estimation result of C_z because thrust is the biggest concern in most modeling tasks. Due to limited space, other models are provided in the appendices.

Table 2 Procedure of identifying the reduced model and the gray-box model

	Reduced model	Gray-box model
Step 1	Data acquisition	
Step 2	Determined structure	Define structure candidates $\mathcal{S}(y)$
Step 3	Parameter estimation	Stepwise regression
	Final model	

Table 3 Estimation results of C_z model, $\mu \le 0.05$

Regressor	$\hat{\theta}$
1	5.020E − 02
$\mu_x^2+\mu_y^2$	1.112E − 01
$(\bar{\nu}_{\text{in}}-\mu_z)^2$	−9.420E − 02
R2	0.953
NRMS	0.021

Table 4 Estimations result of C_z model, $\mu > 0.05$

$\lvert\beta\rvert \in [0, 30]$			$\lvert\beta\rvert \in [30, 60]$			$\lvert\beta\rvert \in [60, 90]$		
Regressor	$\hat{\theta}$	NRMS, %	Regressor	$\hat{\theta}$	NRMS, %	Regressor	$\hat{\theta}$	NRMS, %
1	1.38E − 01	8.636	1	2.20E − 01	8.046	1	1.48E − 01	8.759
$\mu_x^2 + \mu_y^2$	−1.55E − 01	8.487	$\mu_x^2 + \mu_y^2$	−3.62E − 01	7.487	$\mu_x^2 + \mu_y^2$	−2.05E − 01	8.533
$(\bar{\nu}_{\text{in}} - \mu_z)^2$	−4.00E − 01	2.315	$(\bar{\nu}_{\text{in}} - \mu_z)^2$	−6.99E − 01	2.142	$(\bar{\nu}_{\text{in}} - \mu_z)^2$	−4.48E − 01	2.882
μ_z	−1.02E − 01	2.070	μ_z	−2.91E − 01	1.785	μ_z	−1.93E − 01	2.575
$\lvert u_q\rvert\mu_z$	−2.28E − 02	1.995	$\lvert u_p\rVert\mu_y\rvert$	−1.84E − 02	1.723	$\lvert u_p\rvert\mu_z$	4.52E − 02	2.418
$\lvert u_p\rvert\mu_z$	7.83E − 02	1.952	$\lvert u_r\rVert\mu_y\rvert^2\mu_z^2$	3.22E + 00	1.696	μ_z^3	1.08E + 01	2.342
$\lvert u_p\rvert\mu_z^2$	5.88E − 01	1.940	$\lvert u_q\rVert\mu_x\rvert$	1.19E − 02	1.672	μ_z^4	3.70E + 01	2.240
$\lvert u\rvert\mu_z^3$	3.48E + 00	1.928	$\lvert\bar{r}\rVert\mu_y\rvert\mu_z^3$	1.34E + 03	1.655	μ_z^2	5.82E − 01	2.165
$\lvert u_q\rvert$	−3.11E − 04	1.923	$\lvert u_p\rVert\mu_y\rvert^2\mu_z^2$	3.81E + 00	1.650	$\lvert u_p\rVert\mu_y\rvert$	7.06E − 03	2.148
R2	0.9503		R2	0.9580		$\lvert u_p\rVert\mu_y\rvert^3\lvert\mu_z\rvert$	−1.51E + 00	2.139
						R2	0.9403	

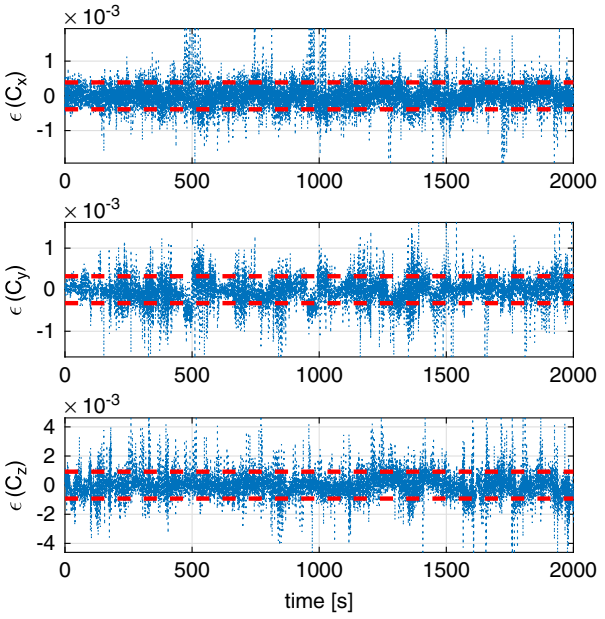

Fig. 12 Residuals of force models compared with the $1 - \sigma$ interval.

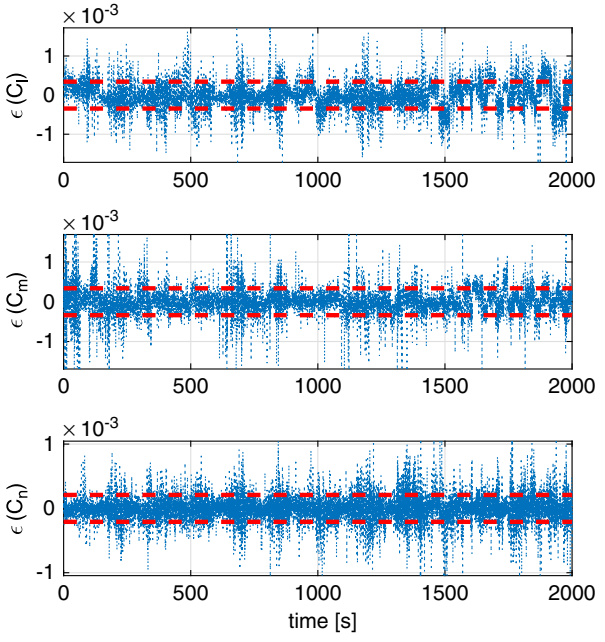

Fig. 13 Residuals of moment models compared with the $1 - \sigma$ interval.

The reduced model is found to be accurate in low-speed regions because the interaction effects are weak. Thus, C_z is estimated with structure (33) when $\mu < 0.05$ (approximately $V < 2$ m/s). The result at this low-speed regime is listed in Table 3.

For the flight regime in which $\mu > 0.05$, the complex aerodynamic effects become apparent and the gray-box model of C_z is established. The model structures and parameters are listed in Table 4. The state space is equally divided into three partitions according to the sideslip angle. On each partition, a gray-box model of C_z is identified. The first column of the table lists the model structure, which is ranked by the order of selection. The second column gives the values of the corresponding parameters. The third column provides the decreasing normalized root mean square (NRMS) of the model residual after the corresponding regressor is added into the model. In general, regressors at the top are the most significant, with significance becoming less moving toward the bottom of the list.

Figures 12 and 13 present the residuals of gray-box models on the entire estimation datasets. Note that $1 - \sigma$ intervals are given as well. In general, the residuals are confined to the interval. This also indicates that the gray-box model provides unbiased estimations because all residuals have a mean value close to zero. The aforementioned properties demonstrate the validity of the model structure selected by the stepwise regression algorithm.

B. Validation Results

Gray-box models are validated using validation data that are separate from the estimation data but are collected from the same flights. For a better evaluation of these models, the validation outputs are chosen as forces and moments instead of their coefficients.

The force models are compared with the reduced models [Eqs. (25) and (32)], which have taken into account primary aerodynamic effects. The moment models, however, are compared with the hovering model because no mature reduced model for moment prediction can be found. The metrics of these models are given in Table 5 based on validation results.

Both the gray-box and reduced models provide accurate F_x and F_y predictions. From the F_z metrics, it can be concluded that the gray-box model provides better thrust estimations. The RMS of the

Table 5 Summary of validation results

	Gray-box model			Reduced or. hovering * model		
	Output corr.	R2	NRMS, %	Output corr.	R2	NRMS, %
F_z	0.9353	0.8636	2.10	0.8831	0.7650	3.03
F_x	0.9945	0.9889	1.54	0.9934	0.9861	1.70
F_y	0.9987	0.9975	1.05	0.9981	0.9961	1.32
M_x	0.7687	0.4847	2.06	0.1994*	−0.0201*	12.63*
M_y	0.8567	0.6883	1.23	0.4141*	−0.0524*	7.53*
M_z	0.8071	0.4873	5.19	0.4152*	0.1417*	13.81*

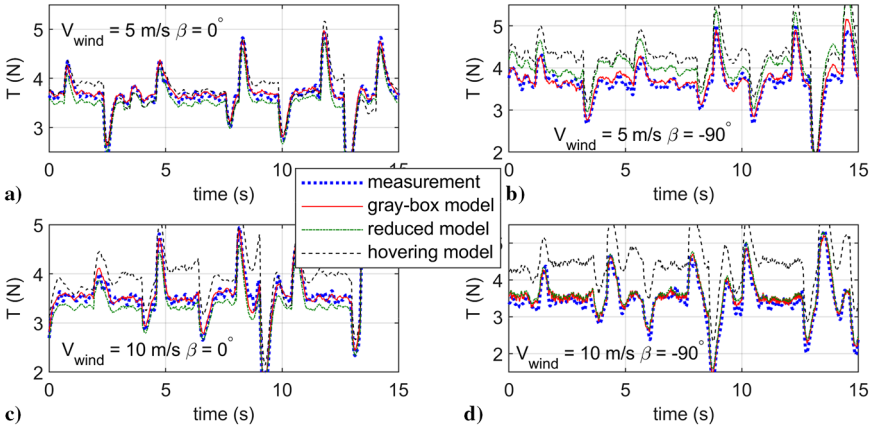

Fig. 14 Validation results of the thrust model.

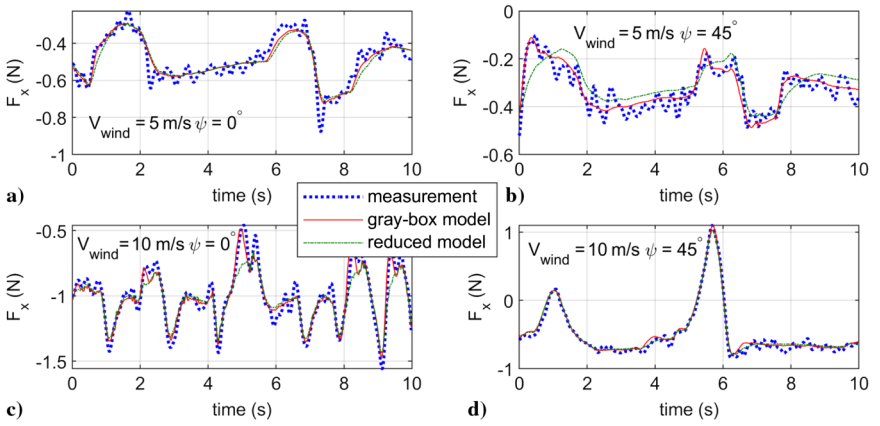

Fig. 15 Validation results of the F_x model.

gray-box force model residuals are reduced by 20–30% on the whole. As for moment predictions, the hovering models (marked by asterisks) are almost invalid, whereas the gray-box models can provide adequate results. Specifically, the RMSs of the residuals are reduced by over 80%. To make detailed a comparison between the aforementioned models, several figures are given in the following.

Figure 14 gives the validation result of F_z, where the thrust $T = -F_z$ is plotted for readability. The gray-box model (red solid line) is compared with the reduced model (green dashed–dotted line) and the hovering model (black dashed line). The left two figures illustrate flights when wind speeds are 5 and 10 m/s and the sideslip angle is zero. The right two figures represent flights when the sideslip angle is 90. The gray-box model outperforms the other models in general. Climbing and descending flights are performed at 5 and 10 m/s airspeeds with $\beta = 0$ and $\beta = -90$ deg, respectively. It is clear that both the gray-box model and the reduced model [Eq. (32)] outperform the hovering model, especially in the high-speed and large sideslip flight regimes. It is evident that the accuracy of the reduced model degrades beyond 5 m/s, which could be caused by disturbances from the interactions of the Bebop fuselage with the airflow.

The drag model has been validated by forward and backward flights with different heading angles ψ. Figure 15 shows the validation results of F_x. The gray-box model (red solid line) is compared with the reduced model (green dashed–dotted line). Forward and backward flights are performed for validation. The left two figures show flights with a zero heading angle (i.e., toward the wind-tunnel outlet), whereas the heading angle is 45 deg in the right two figures. The reduced model [Eq. (25)], neglecting interaction effects, is compared. Although both models perform well in general, the gray-box model is more accurate in certain parts. For example, at $t = 5.0$ s and $t = 8.3$ s in Fig. 15b, the gray-box model provides an accurate prediction, whereas the reduced model produces relatively large errors. The angle of attack and the model residuals of this subplot are given in Fig. 16. It can be seen that the gray-box model

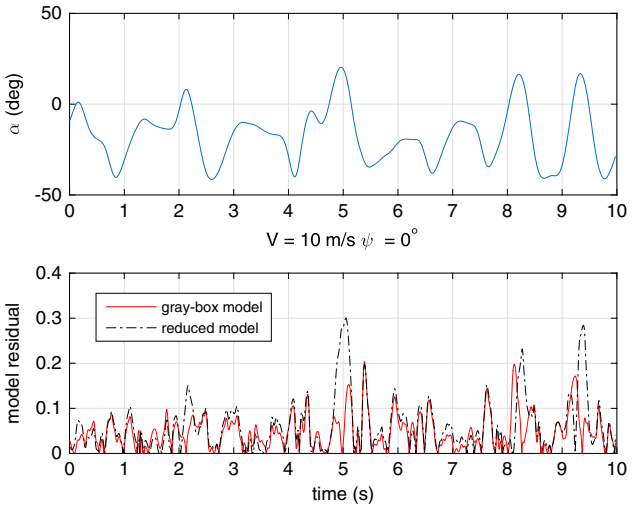

Fig. 16 Time series of angle of attack at $V_{\text{wind}} = 10$ m/s and $\psi = 0$. The angle of attack is positive at $t = 5.0$ s and $t = 8.3$ s when errors in the reduced model for F_x appear.

outperforms the reduced model when the angle of attack is positive, which means that interactions between the front and aft rotors appear and the reduced model becomes less accurate.

Figure 17 provides validation results of the F_y model. The gray-box model (red solid line) is compared with the reduced model (green dashed–dotted line). Forward and backward flights relative to the wind flow are performed. The left two figures present flights with a 90 deg heading angle (i.e., leftward flight against wind flow), whereas the heading angle is 45 deg in the right two figures. In flights with 90 deg heading angles, the quadrotor flew toward the left, as Fig. 3 illustrates. Again, as shown in Fig. 18, the gray-box model

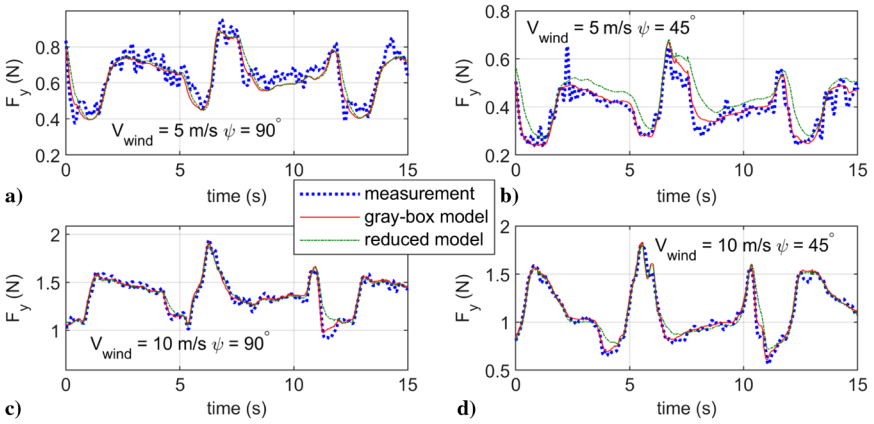

Fig. 17 Validation results of the F_y model.

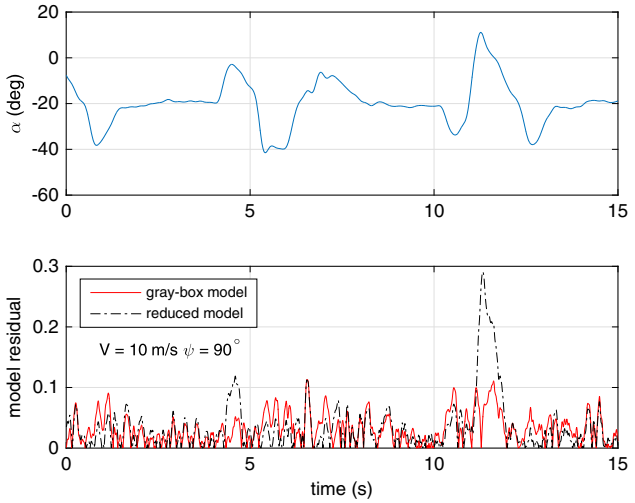

Fig. 18 Time series of angle of attack in $V_{wind} = 10$ m/s and $\psi = 90$ deg. The angle of attack is positive at $t = 12.0$ s when errors of the F_y reduced model appear.

outperforms the reduced model at points when α is above zero. At $t = 12$ s, when the angle of attack is positive, a large error appears in predictions made by the reduced model, which does not take into account aerodynamic interaction effects.

Figure 19 presents the validation result of the pitching moment model. The gray-box model outperforms the hovering model as expected. The gray-box model (red solid line) is compared with the hovering model (black dashed–dotted line). Forward and backward flights relative to the wind flow are used for validation. The left two figures show flights with a zero heading angle (i.e., toward the wind-tunnel outlet), whereas the heading angle is 45 deg in the right figures. During flights with $\psi = 0$, the prediction of the hovering model is almost always smaller than the measurements because the aft rotors need to rotate much faster than front rotors in the trim condition, which is in line with the observation given in Ref. [22]. This phenomenon indicates that, during forward flight, a significant pitchup moment appears that is not considered in the hovering model. As for the flights with $\psi = 45$ deg, although a large aerodynamic coupling exists due to large sideslip angles, the gray-box model can still provide accurate predictions. In addition, validation results of the M_x model are given in Fig. 20, showing the great advantage of the gray-box model.

The model of the yawing moment M_z has been validated by yaw maneuvers and forward–backward maneuvers in the wind tunnel. The forward–backward maneuvers are carried out with $\psi = 45$ deg. As can be seen in Fig. 21, predictions from the gray-box model are more accurate than the hovering model. The residual of the hovering model increases as the flight speed grows, and a constant bias appears in Fig. 21d. In this case, the quadrotor flies with $\psi = 45$ deg; in other words, the negative sideslip angle and additional positive yawing moment appear due to aerodynamic effects.

Finally, the gray-box models have been validated near the hovering condition and compared with the hovering models. As Fig. 22 shows, both types of models are accurate. Because aerodynamic resistance is small as compared to the presented variables in the hovering condition, models of F_x and F_y are omitted in the plot.

The piecewise polynomial model in this research is discontinuous on the boundary of each section that might be unfavorable for some applications, although the discontinuity can be effectively weakened by increasing the number of model segments. More advanced base functions such as multivariate splines may replace polynomials to guarantee the smoothness of the global model.

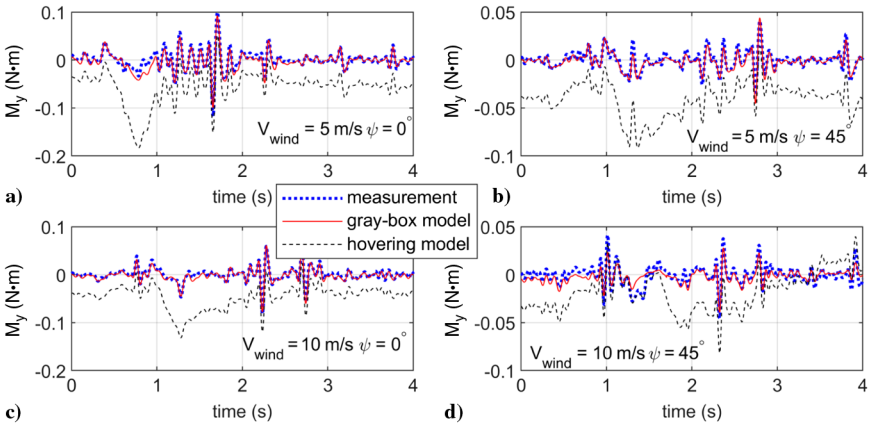

Fig. 19 Validation result of the pitching moment M_y model.

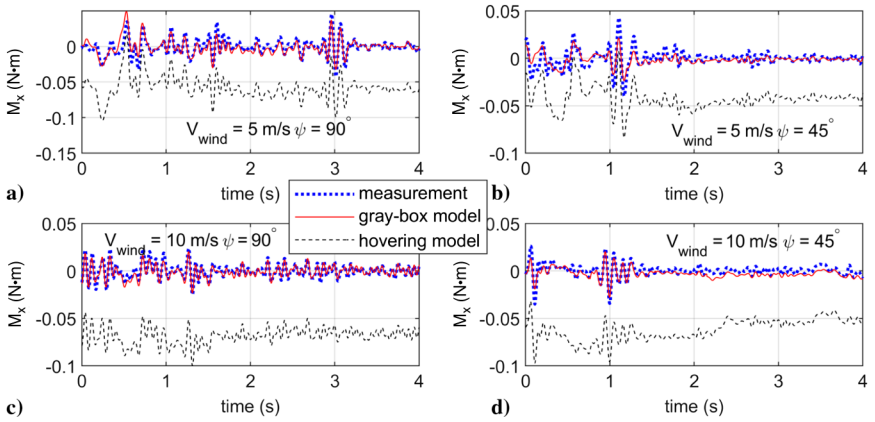

Fig. 20 Validation result of rolling moment M_x model. The gray-box model (red solid) is compared with hovering model (black dash-dot). Forward and backward flights relative to the wind low are performed. The left two figures present flights with 90 deg heading angle, i.e., leftward flight against wind flow, while the heading angle is 45 deg in the right figures.

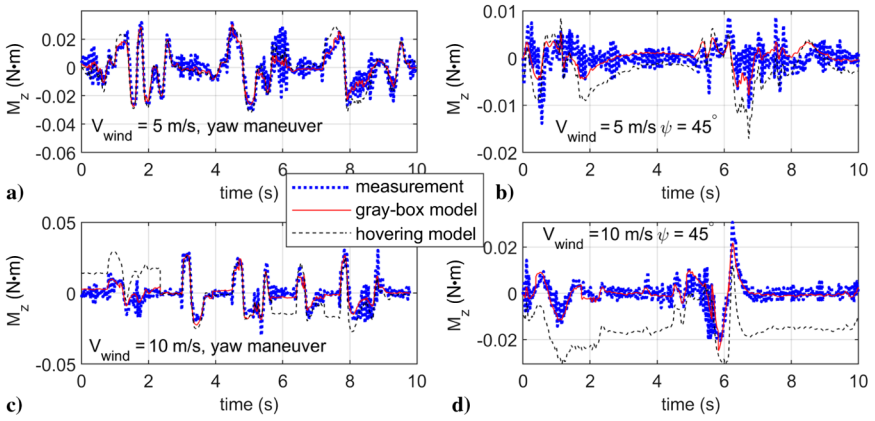

Fig. 21 Validation results of the M_z model. The gray-box model (red solid) is compared with hovering model (black dash-dot). Yaw maneuvers are performed in the left two figures, with different flight speeds. Right two figures present data from forward and backward flights along the wind flow direction with 45 deg heading angle.

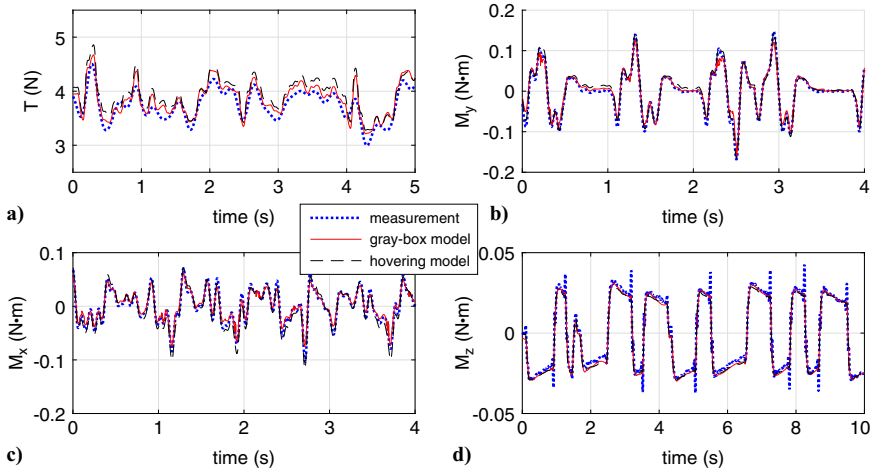

Fig. 22 Validation results during hovering condition. Gray-box model (red solid) is compared with hovering model (green dash-dot). Both model possess enough accuracy in the hovering condition.

VII. Conclusions

Gray-box models of a specific type of quadrotor considering aerodynamic interaction effects have been identified from flight data in a larger flight envelope with respect to the hovering condition. The identification process of this gray-box model consisted of the information of phenomenological observation and prior knowledge about rotorcraft aerodynamics. Therefore, this type of model possessed higher reliability in both high-speed and low-speed flight regimes. Although the model structure and parameters were specific to the Bebop platform, the methodology including nondimensionalization, structure candidates, and the stepwise regression algorithm could be generalized to other multirotor platforms.

The high-speed flight data have been collected in the wind tunnel. These flight data illustrated significant interaction effects that were rarely considered in the previous literature. The thrust reductions of the aft rotors that were obstructed by the front rotors or airframe led to

variations of the thrust, moment, and even drag force acting on the quadrotor, which might inspire the drone manufacturer to revise their design: for instance, increasing the power of aft actuators.

Because the data are obtained from flight tests instead of conventional static wind-tunnel tests, and the forces and moments are measured indirectly from onboard and external navigation sensors, this process can also be applied in the open area instead of the wind tunnel. The motion capture system can be replaced by other navigation sensors, such as Real-time kinematic GPS (RTK-GPS), which can produce accurate velocity and position measurements. Thus, the method introduced in this paper can be repeated without wind-tunnel equipment to establish accurate models in the interested flight regime.

However, on the other hand, a flight test is only able to explore a limited regime of the flight envelope, which is unfavorable for global model identification. The interaction effects can be only partially revealed by free-flight data. Therefore, static wind-tunnel tests with force balance are also suggested for global model identification as well as analyzing interaction effects in detail.

Appendix A: Stepwise Regression Algorithm

The stepwise regression algorithm is summarized in Algorithm A1.

Algorithm A1 Forward–backward stepwise regression algorithm

Set initial regressor matrix $A_0 = [1, 1, \ldots, 1]^T \in \mathbb{R}^N$
Set candidate set $\mathcal{S}(y) = \{\boldsymbol{\xi}_0, \boldsymbol{\xi}_1, \ldots, \boldsymbol{\xi}_q\}$ containing $q + 1$ candidates
$k_{\max} = 30$; $PSE_{\text{tol}} = 10^{-6}$; $F_{\text{out}} = 4$; $k = 0$
$\boldsymbol{\epsilon}_0 = [\boldsymbol{I} - A_0(A_0^T A_0)^{-1} A_0^T]\boldsymbol{z}$
while $k \le k_{\max}$, **do**
%Forward selection%
  $k = k + 1$
  for $i = 0, 1, \ldots, q$, **do**
    $\boldsymbol{\lambda}_i = \boldsymbol{\xi}_i - A_{k-1}(A_{k-1}^T A_{k-1})^{-1} A_{k-1}^T \boldsymbol{z}$
  end for
  $j = \text{argmax}_i \text{corr}(\boldsymbol{\lambda}_i, \boldsymbol{\epsilon}_{k-1})$ ▷ %corr($\boldsymbol{x}$, $\boldsymbol{y}$) stands for the correlation of $\boldsymbol{x}$ and $\boldsymbol{y}$%
  $A_k = [A_{k-1}, \boldsymbol{\xi}_j]$
  $\hat{\boldsymbol{\theta}} = (A_k^T A_k)^{-1} A_k \boldsymbol{z}$
  $\boldsymbol{\epsilon}_k = \boldsymbol{z} - A_k \hat{\boldsymbol{\theta}}_k$
%Backward elimination%
  Assume there has been p regressors added into A_k
  for $i = 1, 2, \ldots, p$, **do**
    Define $A_{k,i}$ as the reduced regressor matrix of A_k of which the ith regressor is eliminated
    $\hat{\boldsymbol{\theta}}_{k,i} = (A_{k,i}^T A_{k,i})^{-1} A_{k,i}^T \boldsymbol{z}$
    $SS_R(\hat{\boldsymbol{\theta}}_k) = \hat{\boldsymbol{\theta}}_k A_k^T \boldsymbol{z} - N\bar{z}^2$ ▷ %$\bar{z}$ stands for the mean of $\boldsymbol{z}$%
    $SS_R(\hat{\boldsymbol{\theta}}_{k,i}) = \hat{\boldsymbol{\theta}}_{k,i} A_{k,i}^T \boldsymbol{z} - N\bar{z}^2$
    $s^2 = \boldsymbol{\epsilon}_k^T \boldsymbol{\epsilon}_k / (N - p - 1)$
    The F0 ratio of the ith regressor can be calculated by
    $F_{0,i} = [SS_R(\hat{\boldsymbol{\theta}}_k) - SS_R(\hat{\boldsymbol{\theta}}_{k,i})]/s^2$
  end for
  $l = \text{argmin}_i F_{0,i}$
  if $F_{0,l} < F_{\text{out}}$, **then** $A_k = A_{k,l}$
    $\hat{\boldsymbol{\theta}} = (A_k^T A_k)^{-1} A_k \boldsymbol{z}$
    $\boldsymbol{\epsilon}_k = \boldsymbol{z} - A_k \hat{\boldsymbol{\theta}}_k$
  end if
%Stopping criteria%
  $PSE = \frac{1}{N} \boldsymbol{\epsilon}_k^T \boldsymbol{\epsilon}_k + \frac{p}{N^2} \sum_{i=1}^{N} [\boldsymbol{z}(i) - \bar{z}]$
  if $PSE > PSE_{\text{last}}$ or $PSE \le PSE_{\text{tol}}$ or $l = j$, **then**
    break
  end if
  $PSE_{\text{last}} = PSE$
end while
A_k is the final regressors matrix (model structure), $\hat{\boldsymbol{\theta}}_k$ is the estimated parameters, and $\boldsymbol{\epsilon}_k$ is the model residual

Table B1 Estimation results of C_x model

$\lvert\beta\rvert \in [0, 30]$ deg			$\lvert\beta\rvert \in [30, 60]$ deg			$\lvert\beta\rvert \in [60, 90]$ deg		
Regressor	$\hat{\theta}$	NRMS, %	Regressor	$\hat{\theta}$	NRMS, %	Regressor	$\hat{\theta}$	NRMS, %
1	4.182E − 04	18.374	1	4.390E − 04	22.466	1	5.007E − 04	9.566
μ_x	−3.482E − 02	1.327	μ_x	−3.684E − 02	2.271	μ_x	−3.873E − 02	3.067
$\mu_x\mu_z$	7.717E − 02	1.232	$\lvert\mu_y\rvert^3$	7.354E − 02	2.213	$\lvert\mu_y\rvert^3$	2.412E − 02	2.983
$\mu_x\mu_z^2$	1.057E + 00	1.157	$\mu_x\mu_z^2$	3.673E + 00	2.190	μ_z	3.956E − 03	2.960
$\mu_x\mu_z^3$	3.837E + 00	1.119	$\mu_x\mu_z$	2.216E − 01	2.111	μ_z^2	3.055E − 02	2.915
$\mu_x^2\mu_z^2$	7.365E − 01	1.101	$\mu_x\mu_z^3$	1.497E + 01	1.929	$\mu_x\mu_z^2$	2.495E − 01	2.904
μ_x^3	−2.883E − 02	1.082	μ_x^3	6.234E − 02	1.918	R2	0.9079	
μ_z^2	−2.073E − 02	1.075	R2	0.9927		— —	— —	— —
R2	0.9966		— —	— —	— —	— —	— —	— —

Table B2 Estimation result of C_y model

$\lvert\beta\rvert \in [0, 30]$ deg			$\lvert\beta\rvert \in [30, 60]$ deg			$\lvert\beta\rvert \in [60, 90]$ deg		
Regressor	$\hat{\theta}$	NRMS, %	Regressor	$\hat{\theta}$	NRMS, %	Regressor	$\hat{\theta}$	NRMS, %
1	−1.79E − 04	6.595	1	−1.98E − 04	16.820	1	−1.23E − 04	16.563
μ_y	−3.36E − 02	2.771	μ_y	−3.54E − 02	1.675	μ_y	−3.88E − 02	1.283
$\mu_y\mu_z$	1.16E − 01	2.718	$\lvert\mu_x\rvert\mu_y\mu_z$	2.56E − 01	1.201	$\mu_y^3\mu_z$	4.41E − 01	0.979
$\mu_x^2\mu_z^2$	9.29E − 01	2.693	$\mu_y\mu_z^3$	4.64E + 00	1.163	$\mu_y\mu_z^3$	1.41E + 00	0.945
$\lvert\mu_x\rvert\mu_z^2$	−2.10E − 01	2.677	$\mu_y\mu_z$	1.61E − 01	1.141	$\mu_y\mu_z$	8.39E − 02	0.877
$\lvert\mu_x\rvert$	5.45E − 04	2.664	$\mu_y\mu_z^2$	1.57E + 00	1.113	$\mu_y\mu_z^2$	7.41E − 01	0.857
R2	0.8368		μ_y^3	−1.05E − 01	1.089	μ_y^3	−7.01E − 02	0.830
— —	— —	— —	$\lvert\mu_x\rvert$	1.14E − 03	1.083	$\mu_y^2\mu_z^2$	1.12E − 01	0.828
— —	— —	— —	R2	0.9959		R2	0.9975	

Table B3 Estimation result of C_m model; $\lvert\beta\rvert \in [0, 45]$ deg

$\lvert\beta\rvert \in [0, 15]$ deg			$\lvert\beta\rvert \in [15, 30]$ deg			$\lvert\beta\rvert \in [30, 45]$ deg		
Regressor	$\hat{\theta}$	NRMS, %	Regressor	$\hat{\theta}$	NRMS, %	Regressor	$\hat{\theta}$	NRMS, %
1	1.16E − 04	6.247	1	5.36E − 05	9.779	1	1.73E − 05	5.456
u_q	4.44E − 03	4.831	u_q	4.70E − 03	6.682	u_q	5.01E − 03	4.490
$u_q\mu_z$	−5.10E − 02	4.589	$u_q\lvert\mu_y\rvert$	−5.31E − 02	4.843	$u_q\lvert\mu_y\rvert$	−9.56E − 02	4.150
μ_x	5.04E − 02	4.414	μ_x	4.32E − 02	3.473	$u_q\mu_y^2$	8.09E − 01	3.168
μ_x^2	1.91E − 02	4.019	$\mu_x^3\mu_z$	5.60E + 00	3.093	μ_x	2.84E − 02	2.988
μ_z	3.57E − 02	3.375	$\mu_x^3\mu_y^2\mu_z$	−5.82E + 02	2.857	$u_q\mu_z$	−6.23E − 02	2.714
$\bar{q}$	−1.35E − 01	3.205	$\mu_x\lvert\mu_y\rvert$	−4.29E − 01	2.650	$\mu_x\mu_z^2$	−5.20E + 00	2.360
μ_x^3	−1.27E + 00	3.072	$u_q\mu_z$	−6.93E − 02	2.512	$u_q\mu_y^2\mu_z$	2.90E + 00	2.154
μ_x^4	2.87E + 00	2.715	$\bar{q}$	−6.94E − 02	2.147	$\mu_x\mu_z^3$	−2.82E + 01	1.947
$u_q\mu_x^2\mu_z$	8.28E − 01	2.500	$u_q\mu_z^2$	−3.25E − 01	2.088	$\bar{q}$	−8.51E − 02	1.768
$u_q\mu_z^3$	9.31E + 00	2.410	R2	0.9521		$u_q\mu_x^3\mu_y^2\mu_z$	3.53E + 02	1.718
$u_q\mu_z^4$	2.25E + 01	2.301	— —	— —	— —	$u_q\mu_z^3$	3.43E + 00	1.619
$\mu_x^2\mu_z$	4.11E − 01	2.234	— —	— —	— —	$u_q\mu_x^2$	1.46E − 01	1.513
$u_q\mu_x\mu_z^3$	−2.31E + 01	2.178	— —	— —	— —	$u_q\mu_x^2\mu_y^2$	−8.85E + 00	1.431
$\mu_x^2\lvert\mu_y\rvert\mu_z^2$	1.90E + 02	2.120	— —	— —	— —	$\mu_y^2\mu_z^5$	−8.23E + 02	1.407
$\mu_x\mu_y^2\mu_z^2$	−7.62E + 02	2.088	— —	— —	— —	R2	0.9393	
R2	0.8872		— —	— —	— —	— —	— —	— —

Table B4 Estimation result of C_m model; $\lvert\beta\rvert \in [45, 90]$ deg

$\lvert\beta\rvert \in [45, 60]$ deg			$\lvert\beta\rvert \in [60, 75]$ deg			$\lvert\beta\rvert \in [75, 90]$ deg		
Regressor	$\hat{\theta}$	NRMS, %	Regressor	$\hat{\theta}$	NRMS, %	Regressor	$\hat{\theta}$	NRMS, %
1	1.97E − 04	3.290	1	−3.82E − 05	4.779	1	−1.75E − 04	3.590
u_q	4.17E − 03	2.837	u_q	4.73E − 03	3.767	u_q	3.67E − 03	2.635
μ_z	3.00E − 03	2.306	μ_x	5.52E − 02	3.605	$\mu_y^2\mu_z$	1.57E − 01	2.615
μ_x	3.74E − 02	2.128	$\mu_x\mu_z^2$	−7.24E + 00	3.400	$u_q\mu_z$	−9.03E − 02	2.598
$\mu_x\lvert\mu_y\rvert\mu_z^2$	7.33E + 00	1.995	$u_q\mu_z$	−7.10E − 02	3.244	$u_q\mu_z^2$	−9.29E − 01	2.562
$u_q\mu_x^2\lvert\mu_y\rvert$	2.42E + 00	1.900	$\mu_x\lvert\mu_y\rvert$	−3.57E − 01	3.100	$\mu_y^2\mu_z^3$	−2.56E + 01	2.512
$u_q\mu_z$	−6.30E − 02	1.845	$u_q\lvert\mu_y\rvert$	−2.66E − 02	2.996	$u_q\lvert\mu_y\rvert\mu_z^4$	−2.17E + 02	2.491
$\mu_x\bar{q}$	−8.64E − 01	1.815	$\mu_x\lvert\mu_y\rvert\mu_z^2$	5.24E + 01	2.800	μ_z	−2.44E − 03	2.470
$u_q\lvert\mu_y\rvert\mu_z^2$	−3.67E + 00	1.788	$\mu_x\mu_y^2\mu_z^2$	−1.02E + 02	2.641	$\lvert\mu_y\rvert\mu_z^5$	2.41E + 02	2.448
$\mu_x\mu_z^2$	−5.88E + 00	1.706	$\mu_x^3\mu_y^2\bar{q}$	−9.88E + 03	2.544	$u_q\mu_z^3$	1.49E + 01	2.435
$u_q\mu_x^2\mu_z$	4.35E + 00	1.653	$u_q\mu_z^2$	−3.92E − 01	2.467	$u_q\mu_z^4$	1.14E + 02	2.402
$u_q\mu_x^3\mu_y^2$	−5.76E + 01	1.631	$\mu_x^3\lvert\mu_y\rvert\mu_z\bar{q}$	−1.77E + 04	2.394	$u_q\lvert\mu_y\rvert$	−1.06E − 02	2.370
$\mu_x\lvert\mu_y\rvert$	−1.03E − 01	1.608	$\bar{q}$	−6.07E − 02	2.360	$u_q\lvert\mu_y\rvert\mu_z^2$	6.79E + 00	2.351
$\mu_x\mu_z^3$	−2.71E + 01	1.550	$u_q\mu_y^2$	8.98E − 02	2.334	$u_q\lvert\mu_y\rvert\mu_z$	2.45E − 01	2.340
$u_q\lvert\mu_y\rvert$	−2.04E − 02	1.517	$u_q\lvert\mu_y\rvert\mu_z$	3.12E − 01	2.315	$\mu_y^2\mu_z^2$	−2.11E + 00	2.307
$u_q\mu_x^3\mu_y^2\mu_z$	−5.26E + 02	1.476	$u_q\mu_x$	−5.50E − 03	2.257	$\lvert\mu_y\rvert\mu_z^4$	2.69E + 01	2.298
$u_q\mu_x^2\lvert\mu_y\rvert\mu_z^2$	8.14E + 01	1.438	$\mu_x\mu_y^2$	5.39E − 01	2.236	μ_x	1.58E − 03	2.292
$u_q\mu_y^2\mu_z^5$	−1.51E + 03	1.425	$\mu_y^2\mu_z$	8.33E − 02	2.185	R2	0.5958	
R2	0.8107		$u_q\lvert\mu_y\rvert\mu_z^2$	1.41E + 00	2.163	— —	— —	— —
— —	— —	— —	$\mu_x\mu_z^3$	−5.46E + 00	— —	— —	— —	— —
— —	— —	— —	R2	0.7782		— —	— —	— —

Table B5 Estimation result of C_l model; $|\beta| \in [0, 45]$ deg

$\|\beta\| \in [0, 15]$ deg			$\|\beta\| \in [15, 30]$ deg			$\|\beta\| \in [30, 45]$ deg		
Regressor	$\hat{\theta}$	NRMS, %	Regressor	$\hat{\theta}$	NRMS, %	Regressor	$\hat{\theta}$	NRMS, %
1	2.30E − 04	2.940	1	1.28E − 04	6.321	1	2.79E − 04	6.603
u_p	5.40E − 03	1.885	u_p	5.08E − 03	3.693	u_p	3.86E − 03	6.251
μ_y	−2.84E − 02	1.825	μ_y	−1.93E − 02	2.695	μ_y	−4.12E − 02	5.089
$\|\mu_x\|\bar{p}$	−3.32E − 01	1.789	$\mu_x^2\mu_y^3\mu_z$	−9.23E + 02	2.186	$\mu_x^2\mu_y$	−2.51E + 00	4.567
$\mu_x^2\mu_y$	5.08E − 01	1.767	μ_y^2	2.56E − 01	2.042	$\|\mu_x\|\mu_y$	5.41E − 01	4.407
$u_p\|\mu_x\|$	−4.44E − 02	1.726	$\|\mu_x\|\mu_y^4$	−1.80E + 02	1.795	$\mu_y^3\mu_z$	2.03E + 01	4.289
$u_p\mu_z$	−1.26E − 02	1.685	$\bar{p}$	−3.72E − 02	1.662	$\mu_x^2\mu_y^3$	4.74E + 01	4.187
$u_p\mu_x^2$	1.47E − 01	1.659	$\mu_z^2\bar{p}$	−8.79E + 00	1.637	$\mu_z\bar{p}$	1.33E + 00	4.048
$u_p\mu_x^2\mu_z^2$	−2.10E + 00	1.629	R2	0.9282		$\|\mu_x\|\mu_y\mu_z^2$	1.54E + 01	3.844
$u_p\mu_y$	−4.37E − 02	1.607	— —	— —	— —	$u_p\mu_y$	4.73E − 03	3.768
$\mu_x^2\mu_y^2$	2.36E + 01	1.584	— —	— —	— —	$\mu_x^2\mu_z^5\bar{p}$	2.70E + 05	3.741
$u_p\mu_y^2$	3.05E + 00	1.550	— —	— —	— —	$\bar{p}$	−4.30E − 02	3.720
$u_p\mu_x^2\mu_y^3$	1.75E + 03	1.537	— —	— —	— —	$u_p\mu_z^2$	2.64E − 02	3.704
$\mu_x^2\mu_y^4$	−8.40E + 03	1.519	— —	— —	— —	R2	0.6859	
$\mu_y^2\bar{p}$	−9.54E + 01	1.510	— —	— —	— —	— —	— —	— —
R2	0.7331		— —	— —	— —	— —	— —	— —

Table B6 Estimation result of C_l model; $|\beta| \in [45, 90]$ deg

$\|\beta\| \in [45, 60]$ deg			$\|\beta\| \in [60, 75]$ deg			$\|\beta\| \in [75, 90]$ deg		
Regressor	$\hat{\theta}$	NRMS, %	Regressor	$\hat{\theta}$	NRMS, %	Regressor	$\hat{\theta}$	NRMS, %
1	3.16E − 04	3.626	1	2.69E − 04	6.058	1	3.34E − 04	3.931
u_p	4.32E − 03	3.551	u_p	4.37E − 03	5.671	u_p	3.99E − 03	3.751
μ_y	−3.45E − 02	2.982	μ_y	−2.36E − 02	4.600	μ_y	−2.24E − 02	3.192
$\|\mu_x\|\mu_y^3\mu_z$	−2.93E + 01	2.670	μ_y^3	2.12E − 01	3.826	μ_y^3	1.34E − 01	2.683
$\|\mu_x\|\mu_y$	4.44E − 01	2.592	$\mu_y\mu_z^2$	2.37E + 00	3.646	$\mu_y\mu_z^2$	1.35E + 00	2.456
$\mu_x^2\mu_y$	−1.54E + 00	2.512	$u_p\mu_y^2\mu_z^2$	−3.61E + 00	3.473	$\mu_y^2\mu_z\bar{p}$	2.20E + 01	2.350
$u_p\mu_z$	1.03E − 02	2.475	$u_p\mu_y^2\mu_z$	−6.41E − 01	3.369	$\bar{p}$	−5.43E − 02	2.187
$\|\mu_x\|\mu_y^2$	−4.09E − 02	2.438	$\mu_y^2\bar{p}$	−3.25E + 00	3.291	$u_p\mu_z^4$	−4.51E + 01	2.159
$\mu_y\mu_z^3$	−7.70E + 00	2.414	$u_p\mu_z^5$	−1.66E + 02	3.154	$u_p\mu_z^3$	−4.36E + 00	2.129
$\|\mu_x\|\mu_y\mu_z^2$	−1.02E + 01	2.382	$\mu_y^3\mu_z$	1.31E + 00	3.124	μ_z	−2.81E − 03	2.087
$\bar{p}$	−5.76E − 02	2.352	$u_p\mu_z^4$	−2.39E + 01	3.050	$u_p\mu_y^2$	4.01E − 02	2.061
μ_y^3	−4.58E − 01	2.325	$\mu_y\mu_z^3$	9.49E + 00	2.965	$u_p\mu_z^5$	−1.31E + 02	2.047
$u_p\mu_z^2$	9.37E − 02	2.305	$u_p\mu_z^2$	−2.79E − 01	2.922	$\mu_y\mu_z^3$	5.11E + 00	2.008
$u_p\|\mu_x\|$	−1.96E − 02	2.288	$u_p\mu_z^3$	−1.14E + 00	2.907	$u_p\mu_y^4$	−3.73E − 01	1.994
$u_p\mu_y^2$	6.65E − 02	2.269	R2	0.7632		$u_p\mu_z^2$	−1.68E − 01	1.975
$\mu_x^2\mu_y^2$	7.15E + 00	2.262	— —	— —	— —	μ_z^2	−2.23E − 02	1.962
R2	0.6031		— —	— —	— —	R2	0.7476	

Table B7 Estimation result of C_n model, $\mu \leq 0.05$

Regressor	$\hat{\theta}$	NRMS, %
1	2.188E − 05	13.930
$s(u_r)u_r^2$	2.032E − 04	3.382
r	−3.317E − 02	2.689
u_r	3.099E − 04	2.492
$\mu_x^2 r$	3.271E + 02	2.460
R2	0.9690	

Table B8 Estimation results of C_n model; $\mu > 0.05$

$\lvert\beta\rvert \in [0, 30]$ deg			$\lvert\beta\rvert \in [30, 60]$ deg			$\lvert\beta\rvert \in [60, 90]$ deg		
Regressor	$\hat{\theta}$	NRMS, %	Regressor	$\hat{\theta}$	NRMS, %	Regressor	$\hat{\theta}$	NRMS, %
1	5.470E − 05	7.245	1	1.350E − 05	7.120	1	2.202E − 05	8.291
u_r	6.976E − 04	3.446	u_r^3	−4.156E − 05	5.883	u_r^3	3.320E − 05	6.842
$u_r\mu_x$	−5.354E − 04	3.353	$u_r\mu_x$	−3.286E − 04	5.471	$\mu_x\mu_y$	−4.661E − 02	6.280
$\mu_y\mu_z$	4.554E − 02	3.276	$\mu_x\mu_y^3$	−2.113E − 01	5.368	$s(u_r)u_r^2$	−7.975E − 05	6.170
$s(r)\bar{r}^2$	−1.781E + 00	3.244	μ_y^3	−2.595E − 02	5.100	μ_y	−1.640E − 03	5.702
R2	0.8060		$s(u_r)u_r^2$	3.005E − 04	4.485	u_r	4.716E − 04	5.445
— —	— —	— —	$\mu_x\mu_x$	1.349E − 02	4.413	$s(\bar{r})\bar{r}^2$	−2.994E + 00	5.366
— —	— —	— —	$s(\mu_y)\mu_y^2\mu_z$	2.348E − 01	4.335	$\mu_x\mu_y\mu_z$	−1.210E − 01	5.352
— —	— —	— —	$u_r\mu_z$	−4.223E − 03	4.245	R2	0.5859	
— —	— —	— —	$s(\bar{r})\bar{r}^2u_r$	5.652E + 01	4.188	— —	— —	— —
— —	— —	— —	$s(u_r)u_r\mu_z$	1.287E − 03	4.156	— —	— —	— —
— —	— —	— —	$\mu_y\mu_z^2$	1.188E − 01	4.141	— —	— —	— —
— —	— —	— —	R2	0.6652			— —	— —

Appendix B: Estimated Model of C_x, C_y, C_m, C_l, and C_n

The estimated aerodynamic coefficients are given in this appendix (Tables B1–B8). Note that the model structure and the corresponding parameters are only applicable to Parrot Bebop without bumpers.

References

[1] Mellinger, D., Michael, N., and Kumar, V., "Trajectory Generation and Control for Precise Aggressive Maneuvers with Quadrotors," *Springer Tracts in Advanced Robotics*, Vol. 79, 2014, pp. 361–373. doi:10.1007/978-3-642-28572-1

[2] Hehn, M., and Dandrea, R., "Real-Time Trajectory Generation for Quadrocopters," *IEEE Transactions on Robotics*, Vol. 31, No. 4, 2015, pp. 877–892. doi:10.1109/TRO.2015.2432611

[3] Smeur, E. J., De Croon, G. C., and Chu, Q., "Gust Disturbance Alleviation with Incremental Nonlinear Dynamic Inversion," *IEEE International Conference on Intelligent Robots and Systems*, Vol. 2016, Nov. 2016, pp. 5626–5631. doi:10.1109/IROS.2016.7759827

[4] Huang, H., Hoffmann, G. M., Waslander, S. L., and Tomlin, C. J., "Aerodynamics and Control of Autonomous Quadrotor Helicopters in Aggressive Maneuvering," *Proceedings of the IEEE International Conference on Robotics and Automation*, IEEE Publ., Piscataway, NJ, 2009, pp. 3277–3282. doi:10.1109/ROBOT.2009.5152561

[5] Alexis, K., Nikolakopoulos, G., and Tzes, A., "Switching Model Predictive Attitude Control for a Quadrotor Helicopter Subject to Atmospheric Disturbances," *Control Engineering Practice*, Vol. 19, No. 10, 2011, pp. 1195–1207. doi:10.1016/j.conengprac.2011.06.010

[6] Leishman, R. C., MacDonald, J. C., Beard, R. W., and McLain, T. W., "Quadrotors and Accelerometers: State Estimation with an Improved Dynamic Model," *IEEE Control Systems*, Vol. 34, No. 1, 2014, pp. 28–41. doi:10.1109/MCS.2013.2287362

[7] Carroll, T., George, I.-R. E., and Bramesfeld, G., "Design Optimization of Small Rotors in Quad-Rotor Configuration," *54th AIAA Aerospace Sciences Meeting*, AIAA Paper 2016-1788, 2016. doi:10.2514/6.2016-1788

[8] Foster, J. V., and Hartman, D., "High-Fidelity Multi-Rotor Unmanned Aircraft System (UAS) Simulation Development for Trajectory Prediction Under Off-Nominal Flight Dynamics," *17th AIAA Aviation Technology, Integration, and Operations Conference*, AIAA Paper 2017-3271, 2017. doi:10.2514/6.2017-3271

[9] Zhang, Y., de Visser, C. C., and Chu, Q. P., "Aircraft Damage Identification and Classification for Database-Driven Online Flight-Envelope Prediction," *Journal of Guidance, Control, and Dynamics*, Vol. 41, No. 2, 2018, pp. 449–460. doi:10.2514/1.G002866

[10] Hoffmann, G. M., Huang, H., Waslander, S. L., and Tomlin, C. J., "Quadrotor Helicopter Flight Dynamics and Control: Theory and Experiment," AIAA Paper 2007-6461, Aug. 2007, pp. 1–20. doi:10.2514/6.2007-6461

[11] Hoffmann, G. M., Huang, H., Waslander, S. L., and Tomlin, C. J., "Precision Flight Control for a Multi-Vehicle Quadrotor Helicopter Testbed," *Control Engineering Practice*, Vol. 19, No. 9, 2011, pp. 1023–1036. doi:10.1016/j.conengprac.2011.04.005

[12] Martin, P., and Salaün, E., "The True Role of Accelerometer Feedback in Quadrotor Control," *Proceedings of the IEEE International Conference on Robotics and Automation*, IEEE Publ., Piscataway, NJ, 2010, pp. 1623–1629. doi:10.1109/ROBOT.2010.5509980

[13] Kaya, D., and Kutay, A. T., "Aerodynamic Modeling and Parameter Estimation of a Quadrotor Helicopter," *AIAA Atmospheric Flight Mechanics Conference*, AIAA Paper 2014-2558, 2014. doi:10.2514/6.2014-2558

[14] Orsag, M., and Bogdan, S., "Influence of Forward and Descent Flight on Quadrotor Dynamics," *Recent Advances in Aircraft Technology*, InTech, London, 2012, pp. 141–156. doi:10.5772/37438

[15] Tang, Y. R., and Li, Y., "Dynamic Modeling for High-Performance Controller Design of a UAV Quadrotor," *2015 IEEE International Conference on Information and Automation*, IEEE Publ., Piscataway, NJ, 2015, pp. 3112–3117. doi:10.1109/ICInfA.2015.7279823

[16] Schulz, M., Augugliaro, F., Ritz, R., and D'Andrea, R., "High-Speed, Steady Flight with a Quadrocopter in a Confined Environment Using a Tether," *IEEE International Conference on Intelligent Robots and Systems*, Vol. 2015, IEEE Publ., Piscataway, NJ, Dec. 2015, pp. 1279–1284. doi:10.1109/IROS.2015.7353533

[17] Gill, R., and Andrea, R. D., "Propeller Thrust and Drag in Forward Flight," *IEEE Conference on Control Technology and Applications (CCTA)*, IEEE Publ., Piscataway, NJ, 2017, pp. 73–79. doi:10.1109/CCTA.2017.8062443

[18] Khan, W., and Nahon, M., "Toward an Accurate Physics-Based UAV Thruster Model," *IEEE/ASME Transactions on Mechatronics*, Vol. 18, No. 4, 2013, pp. 1269–1279. doi:10.1109/TMECH.2013.2264105

[19] Mahony, R., Kumar, V., and Corke, P., "Multirotor Aerial Vehicles: Modeling, Estimation, and Control of Quadrotor," *IEEE Robotics and Automation Magazine*, Vol. 19, No. 3, 2012, pp. 20–32. doi:10.1109/MRA.2012.2206474

[20] Bristeau, P., Martin, P., Salaun, E., and Petit, N., "The Role of Propeller Aerodynamics in the Model of a Quadrotor UAV," *2009 European Control Conference (ECC)*, IEEE Publ., Piscataway, NJ, 2009, pp. 683–688. doi:10.23919/ECC.2009.7074482

[21] Pounds, P., Mahony, R., and Corke, P., "Modelling and Control of a Large Quadrotor Robot," *Control Engineering Practice*, Vol. 18, No. 7, 2010, pp. 691–699. doi:10.1016/j.conengprac.2010.02.008

[22] Russell, C., Jung, J., Willink, G., and Glasner, B., "Wind Tunnel and Hover Performance Test Results for Multicopter UAS Vehicles,"

American Helicopter Society 72nd Annual Forum, American Helicopter Soc., West Palm Beach, FL, 2016.

[23] Luo, J., Zhu, L., and Yan, G., "Novel Quadrotor Forward-Flight Model Based on Wake Interference," *AIAA Journal*, Vol. 53, No. 12, 2015, pp. 3522–3533. doi:10.2514/1.J053011

[24] Morelli, E. A., "Global Nonlinear Aerodynamic Modeling Using Multivariate Orthogonal Functions," *Journal of Aircraft*, Vol. 32, No. 2, 1995, pp. 270–277. doi:10.2514/3.46712

[25] Klein, V., and Morelli, E. A., *Aircraft System Identification: Theory and Practice*, AIAA, Reston, VA, 2006, pp. 141–158. doi:10.2514/4.861505

[26] Lombaerts, T., "Fault Tolerant Flight Control: A Physical Model Approach," Ph.D. Thesis, Delft Univ. of Technology, Delft, The Netherlands, 2010.

[27] Armanini, S. F., Karásek, M., de Croon, G. C. H. E., and de Visser, C. C., "Onboard/Offboard Sensor Fusion for High-Fidelity Flapping-Wing Robot Flight Data," *Journal of Guidance, Control, and Dynamics*, Vol. 40, No. 8, 2017, pp. 2121–2132. doi:10.2514/1.G002527

[28] Smeur, E. J. J., Chu, Q., and de Croon, G. C., "Adaptive Incremental Nonlinear Dynamic Inversion for Attitude Control of Micro Aerial Vehicles," *Journal of Guidance, Control, and Dynamics*, Vol. 39, No. 3, 2016, pp. 450–461. doi:10.2514/1.G001490

[29] Mendes, A., van Kampen, E., Remes, B., and Chu, Q. P., "Determining Moments of Inertia of Small UAVs: A Comparative Analysis of an Experimental Method Versus Theoretical Approaches," *AIAA Guidance, Navigation, and Control Conference*, AIAA Paper 2012-4463, 2012. doi:10.2514/6.2012-4463

[30] Powers, C., Mellinger, D., Kushleyev, A., Kothmann, B., and Kumar, V., *Influence of Aerodynamics and Proximity Effects in Quadrotor Flight, Springer Tracts in Advanced Robotics*, Springer International, Heidelberg, 2013, pp. 289–302. doi:10.1007/978-3-319-00065-7